

# Impact of the noise knowledge uncertainty for the science exploitation of cosmological and astrophysical stochastic gravitational wave background with LISA

Martina Muratore<sup>1</sup>,\* Jonathan Gair<sup>1</sup>, and Lorenzo Speri<sup>1</sup>

*Max Planck Institute for Gravitational Physics (Albert Einstein Institute), D-14476 Potsdam, Germany*

 (Received 3 August 2023; accepted 7 December 2023; published 7 February 2024)

This paper investigates the impact of a lack of knowledge of instrumental noise on the characterization of stochastic gravitational wave backgrounds with the Laser Interferometer Space Antenna (LISA). We focus on constraints on modeled backgrounds that represent the possible backgrounds from the mergers of binary black holes of stellar origin, from primordial black hole generation, from nonstandard inflation, and from sound wave production during cosmic fluid phase transitions. We use splines to model generic, slowly varying, uncertainties in the auto- and cross-spectral densities of the LISA time delay interferometry channels. We find that allowing for noise knowledge uncertainty in this way leads to 1–2 orders of magnitude degradation in our ability to constrain stochastic backgrounds and a corresponding increase in the background energy density required for a confident detection. We also find that, to avoid this degradation, the LISA noise would have to be known at the subpercent level, which is unlikely to be achievable in practice.

DOI: [10.1103/PhysRevD.109.042001](https://doi.org/10.1103/PhysRevD.109.042001)

## I. INTRODUCTION

The Laser Interferometer Space Antenna (LISA) is part of the European Space Agency (ESA) Cosmic Vision program and is due to be launched in the mid-2030s. LISA will be the first observatory in space to study gravitational waves (GWs) at millihertz frequencies. It will consist of a constellation of three satellites forming a quasiequilateral triangle and continuously exchanging laser beams [1]. LISA is expected to observe a large variety of sources, such as galactic binaries (GBs), massive black hole binaries [2], stellar-origin black hole binaries [3–5], extreme-mass-ratio inspirals [6], and possibly stochastic backgrounds arising from astrophysical and cosmological processes [7].

When considering the science that can be done with LISA, it is typical to assume a known model for the instrumental noise in the detector data channels. However, these noise levels will not be known in practice. This is also true for ground-based gravitational wave detectors, but in that context spectral density estimation is easier because signals are rare and short-lived, allowing the spectral density to be estimated from data in the vicinity of observed

events. LISA signals, by contrast, are typically long-lived, which means that noise and signal properties must be simultaneously estimated by fitting a suitable model. While such methods and models are still under development, it is expected that the characterization of deterministic signals will not be significantly affected by lack of instrumental noise knowledge (see Appendix B 4). The case of stochastic GW backgrounds (SGWBs) is different, however, as these are intrinsically of the same character as the stochastic instrumental noise. Searches for stochastic signals in ground-based interferometers rely on the cross-correlation of data from independent detectors [8]. This would be possible only if there is another space-based interferometer in operation concurrently, such as Taiji [9], but this is not certain at the moment. In the case of ground-based detectors like LIGO, cross-correlating different detectors can be advantageous, as it helps to retrieve the common gravitational wave signal and isolate it from the independent noise sources in each detector [10]. However, for space-based detectors like LISA, the instrumental noise in one channel can be correlated with the instrumental noise in another channel, making it challenging to find completely independent or orthogonal channels [11]. As a result, our paper focuses on addressing the specific challenges associated with distinguishing between the stochastic instrumental noise and a stochastic gravitational wave signal in the context of LISA. We do this using the Fisher matrix formalism [12–14].

One approach is to use a model for the instrumental noise. It is possible to derive analytical models that describe

\*martina.muratore@aei.mpg.de

*Published by the American Physical Society under the terms of the Creative Commons Attribution 4.0 International license. Further distribution of this work must maintain attribution to the author(s) and the published article's title, journal citation, and DOI. Open access publication funded by the Max Planck Society.*

how different known noise sources propagate into the LISA data stream. However, not all noise sources will be known in advance, so we will not be able to strictly rely on the models, as we cannot perform full tests and directly measure the noise. In the LISA-Pathfinder (LPF) mission [15] for instance, it was seen that the analytical models could not fully explain the measured noise at low frequency. The LISA hardware should be similar to LPF, at least for the gravitational reference sensor (GRS), apart from some small changes to accommodate the GRS in the LISA movable optical subassembly [1]. Therefore, when we plan for LISA data analysis, we must be prepared for uncertainty in the noise models.

The goal of this paper is to assess the impact of lacking a noise model for LISA in the parameter estimation of SGWBs. We consider four different models of cosmological and astrophysical SGWBs: a power law to model signals from stellar-origin binary black hole inspirals, a Gaussian bump to model a background from primordial black hole generation, a power law with running to model background from nonstandard inflation, and, finally, a first-order phase transition model, representing GW production from sound waves in the cosmic fluid generated by colliding phase transition bubbles [7].

For each model, we investigate the SGWB parameter measurement precision using the Fisher matrix formalism. We explore how such precision varies as a function of the background energy density with and without the inclusion of instrumental noise uncertainties.

We represent our lack of knowledge of the LISA instrumental noise by multiplying a set of reference auto- and cross-spectral densities with cubic splines. For the reference spectral densities we use the noise model from [1], which includes only the so-called secondary noises [16], the test mass (TM) acceleration and optical metrology noise (OMS). This noise model assumes that the laser noise [17], clock noise [18], and tilt to length coupling [19,20] have been suppressed by the initial noise reduction pipeline [21,22]. To represent the fact that we will have some amount of information from noise modeling before launch, we place a Gaussian prior on the weights of the cubic spline. By varying the Gaussian variance, we explore the effect of having more or less knowledge of the noise.

Several previous studies have tackled the problem of detecting a SGWB with LISA and distinguishing it from the noise, but these have used different methods than the one we employ in this paper. In [23] it was shown that SGWB reconstruction was possible for generic SGWB models if the LISA instrumental noise can be represented by just two parameters, representing the level of TM and OMS noise, assumed equal for all arms of the interferometer. The authors of [11,24] allowed the TM and OMS noises to differ from arm to arm but still assumed that these noises had a known spectral shape as a function of frequency. In [25] an arbitrary noise shape was allowed,

described by a spline, but using a simplified noise model for the single link. Finally, [16] derived an upper bound on the detectable SGWB amplitude when being agnostic on both the signal and noise shape and discussed limitations of the utility of the null channel for distinguishing between instrumental noise and a stochastic GW background.

The paper is organized as follows: In Sec. II, we introduce the general data model that we use in the analysis, and we describe the Fisher matrix formalism that will be used for this work. In Sec. II C, we describe the spline model that we use to represent the uncertainties in the power spectral density (PSD) and cross-spectral density (CSD) of the instrumental noise. In Sec. II D, we give the analytical noise model for a single LISA link that is used as the reference model and the corresponding PSDs and CSDs for the time delay interferometry (TDI) channels  $A$ ,  $E$ , and  $\zeta$ . In Sec. II E, we describe how a stochastic signal appears in the three TDI channels and their cross-correlations, while in Sec. II F, we describe the models for the cosmological and astrophysical SGWBs that we use in this paper. In Sec. III A, we show how well we can estimate the parameters of the different SGWB models when we allow for uncertainty in our knowledge of the instrumental noise. For each model, we compare the precision of parameter estimation to that when noise knowledge is perfect and show how the parameter precisions vary as a function of the background energy density,  $\Omega$ , evaluated at 1 mHz. In Sec. III B, we show how the results change as we vary our priors uncertainty on the instrumental noise. We conclude our results in Sec. III C by showing how well the signal, noise, and galactic foreground can be reconstructed for a power law SGWB background. Section IV summarizes our conclusions and future perspectives.

## II. METHODS

### A. Likelihood

We assume that the output of a gravitational wave detector,  $s(t)$ , is expressed as a linear combination of a signal,  $h(t|\vec{\mu})$ , determined by a finite set of (unknown) parameters  $\vec{\mu}$  and instrumental noise  $n(t)$ . If we ignore the presence of calibration errors [26], the content of a single data stream, i.e., one output channel from one detector, can be written in the frequency domain as

$$\tilde{s}(f) = \tilde{h}(f|\vec{\mu}) + \tilde{n}(f), \quad (1)$$

where the tilde indicates the Fourier transform. The likelihood for the observed data can be written as  $p(\tilde{s}(f)|\vec{\mu}) = p(\tilde{n}(f) = \tilde{s}(f) - \tilde{h}(f|\vec{\mu}))$ . In a gravitational wave context, it is usual to further assume that the instrumental noise follows a Gaussian distribution characterized by a one-sided PSD,  $S_n(f)$ , defined such that

$$\mathbb{E}[\tilde{n}^*(f)\tilde{n}(f')] = \frac{1}{2}S_n(f)\delta(f-f'), \quad (2)$$

for  $f, f' > 0$ , where the expectation value  $\mathbb{E}$  is taken over the data-generating process. The delta function in the previous equation implies that different frequencies are not correlated.

In reality, the noise model is not known perfectly and could vary from the assumption above in several ways. For example, the PSD might have a different shape from the reference one [27], the probability distribution of the noise might not be Gaussian, or the noise might not be stationary, leading to correlations between frequencies.

In this work, we will continue to assume that the noise is Gaussian and stationary, but we will allow the power spectral density to vary using a parametrized spectral density  $S_n(f) \rightarrow S_n(f|\vec{\lambda})$ , described by parameters  $\vec{\lambda}$ . Then the log-likelihood depends on both sets of parameters,  $\vec{\mu}$  and  $\vec{\lambda}$ , and can be written as

$$l := \ln p(\tilde{s}|\vec{\mu}, \vec{\lambda}) = - \sum_{k=1}^n \ln \left[ 2\pi \frac{S_n(f_k|\vec{\lambda})}{4\Delta f} \right] - \frac{1}{2} \sum_{k=1}^n \frac{|\tilde{s}(f_k) - \tilde{h}(f_k|\vec{\mu})|^2}{\frac{1}{4\Delta f} S_n(f_k|\vec{\lambda})}, \quad (3)$$

where the sum is performed over  $n$  frequencies and  $\tilde{n}(f_k) = \tilde{s}(f_k) - \tilde{h}(f_k|\vec{\mu})$  are the discrete Fourier component at frequency  $f_k = k\Delta f$ , of the data minus signal model. The frequency bin width  $\Delta f$  is related to the total observation time as  $T = 1/\Delta f$ . The first term does not include the  $1/2$  factor, because the real and imaginary parts of  $\tilde{n}(f_k)$  are independent random variables. This follows from the fact that, for a real-time series,  $\tilde{n}^*(f) = \tilde{n}(-f)$ , which combined with Eq. (2) means that  $\langle \tilde{n}(f)\tilde{n}(f') \rangle = 0$  for  $f, f' > 0$ . This allows Eq. (2) to be rewritten as

$$\langle \text{Re}[\tilde{n}(f_k)]^2 \rangle = \langle \text{Im}[\tilde{n}(f_k)]^2 \rangle = \frac{\langle |\tilde{n}(f_k)|^2 \rangle}{2} = \frac{S_n(f_k|\vec{\lambda})}{4\Delta f} \quad (4)$$

for a discrete set of frequencies.

Stochastic gravitational wave backgrounds are not deterministic signals and can be treated on the same footing as the instrumental noise by defining the total variance at frequency  $f_k$  as

$$S_t(f_k|\vec{\theta}, \vec{\lambda}) = S_{\text{GW}}(f_k|\vec{\theta}) + S_n(f_k|\vec{\lambda}). \quad (5)$$

If we assume that all the deterministic sources have been correctly subtracted from the data stream  $s$ , the log-likelihood becomes

$$l(\vec{\theta}, \vec{\lambda}) = - \sum_{k=1}^n \ln \left[ T\pi \frac{S_t(f_k|\vec{\theta}, \vec{\lambda})}{2} \right] - \frac{1}{2} \sum_{k=1}^n \frac{|\tilde{s}(f_k)|^2}{\frac{T}{4} S_t(f_k|\vec{\theta}, \vec{\lambda})}. \quad (6)$$

The derivation of this likelihood can be found in Appendix A.

## B. Fisher matrix

We are interested in understanding the impact of noise knowledge uncertainties on the parameter measurement precision of SGWB. The Fisher information matrix provides a lower bound on the covariance of an unbiased estimator of the model parameters and provides a good approximation to the precision of parameter estimation in the high signal-to-noise ratio limit. We will therefore use it to quantify our ability to measure both the noise parameters  $\vec{\lambda}$  and the background parameters  $\vec{\theta}$ .

In a general context, the Fisher matrix is defined by

$$\Gamma_{ij} = \mathbb{E} \left[ \frac{\partial l}{\partial v^i} \frac{\partial l}{\partial v^j} \right] = -\mathbb{E} \left[ \frac{\partial^2 l}{\partial v^i \partial v^j} \right], \quad (7)$$

where the expectation value  $\mathbb{E}$  is taken over the probability density of the likelihood, which defines the data-generation process or the noise distribution. The partial derivatives are taken with respect to the parameters  $\vec{v}$  on which the likelihood depends. We want to compute the Fisher matrix on the extended parameter space  $\vec{v} = \{\vec{\theta}, \vec{\lambda}\}$ .

It can be shown that the expectation value of the product between the derivative of the log-likelihood for deterministic and stochastic parameters is zero. Therefore, at the level of the Fisher matrix approximation it can be shown that the estimation of the noise and deterministic signal parameters is independent (see Appendix B 4).

For SGWBs, we can compute the Fisher matrix in the continuous frequency domain as

$$\Gamma_{ij} = T \int_0^\infty (\Sigma^{-1})_{lr} \frac{\partial \Sigma^{rp}}{\partial v^i} (\Sigma^{-1})_{pm} \frac{\partial \Sigma^{ml}}{\partial v^j} df \quad (8)$$

with

$$\Sigma(f|\vec{v} = \{\vec{\theta}, \vec{\lambda}\}) = \frac{1}{2} \begin{pmatrix} S_t^{AA} & S_t^{AE} & S_t^{A\zeta} \\ S_t^{AE*} & S_t^{EE} & S_t^{E\zeta} \\ S_t^{A\zeta*} & S_t^{E\zeta*} & S_t^{\zeta\zeta} \end{pmatrix}, \quad (9)$$

where each element of the matrix can be written as a sum of an instrumental noise component and a stochastic gravitational wave component as indicated in Eq. (5). A complete derivation of this formula can be found in Appendix B.

Prior knowledge of the noise can be incorporated by imposing a prior on the instrumental parameters  $\vec{\lambda}$ . When doing numerical marginalization, any prior can be imposed. However, if we approximate the likelihood using a Gaussian distribution, by setting the covariance matrix equal to the inverse of the Fisher matrix, it is convenient to use Gaussian priors. This allows one to use the conjugacy properties of Gaussian distributions and obtain a closed-form expression for the posterior distribution on the parameters, as another Gaussian distribution. This property allows us to explore the measurement precision very efficiently over a wide range of backgrounds and instrumental parameters, as also demonstrated in [26] in the context of understanding the impact of LISA calibration uncertainties. For the background parameters, we assume a Gaussian prior with infinite variance, so that we do not place any constraints on their range. For the instrumental parameters, we assume a normal prior with zero mean and covariance given by  $(\Theta^{\lambda\lambda})^{-1}$ . This is a flexible prior choice, since it permits us to describe a range of noise knowledge scenarios: from totally unknown instrumental noise ( $\Theta = 0$ ) to perfectly known instrumental noise ( $\Theta \rightarrow \infty$ ). The posterior covariance is then given by the inverse of the modified Fisher matrix:

$$\Gamma = \begin{pmatrix} \Gamma^{\theta\theta} & \Gamma^{\theta\lambda} \\ (\Gamma^{\theta\lambda})^\top & \Gamma^{\lambda\lambda} + \Theta^{\lambda\lambda} \end{pmatrix}. \quad (10)$$

The diagonal elements of the inverse of this matrix provide estimates for the precision with which the corresponding parameters can be measured. The estimated precision of measurement of the SGWB parameters accounting for noise model uncertainty is, thus, given by the diagonal elements of the matrix:

$$\sigma_\theta = \sqrt{\text{diag}[(\Gamma^{\theta\theta} - \Gamma^{\theta\lambda}(\Gamma^{\lambda\lambda} + \Theta^{\lambda\lambda})^{-1}(\Gamma^{\theta\lambda})^\top)^{-1}]}. \quad (11)$$

Note that in the limit in which the instrumental noise parameters are perfectly known and the measurement precision of the SGWB parameters is given by  $\sigma_\theta = \sqrt{\text{diag}[(\Gamma^{\theta\theta})^{-1}]}$ .

### C. Modeling noise knowledge uncertainties

To model noise uncertainties, we allow the PSD and CSD of the instrumental channels to deviate from the design specification. However, we assume that such deviations vary smoothly over a relatively wide range of frequencies and model the noise uncertainties as fractional deviations from the design PSD or CSD that are described by natural cubic splines. We write the PSD of the instrumental noise in each channel as

$$S_n(f|\vec{\lambda}) = S_{\text{des}}(f)10^{C(f|\vec{\lambda})}, \quad (12)$$

where  $C(f|\vec{\lambda})$  is a natural cubic spline in  $\log_{10}(f)$ . The parameters  $\vec{\lambda}$  specify the values of the spline at the knots. In this study, we use knots evenly spaced in  $\log_{10}(f)$  between  $\log_{10}(f) = -4$  and  $\log_{10}(f) = 0$ , and we fix the number of knots to 13. Noise curves corresponding to this model, with the weights at each knot drawn randomly from a  $\log_{10}(f) \sim U[-1, 1]$  distribution, are shown in Fig. 1. The figure illustrates the kind of noise variations that this model can capture. We note that the model can capture only noise variations that change smoothly as a function of frequency, but this is in accordance with the behavior of the excess noise [28] that was observed in the LPF data. In LPF, the transient noise variations were identified as glitches and fitted with an *ad hoc* exponential model [29]. As calibration and performance noise model studies for LISA become more advanced, we will have a better idea of what kind of features to include, but, for the moment, we will use the type of noise fluctuations observed in LPF as a reference.

Furthermore, it is noteworthy that the prior choice we have made allows for an approximate one order of magnitude variation in the PSD. This decision is influenced by experimental observations, in which the measurement noise is generally seen to fluctuate within a factor of  $\pm 2$  compared to the model. It is also informed by measurements on LISA-Pathfinder, where the measured noise could be accounted for only within a factor of 2 by the individual noise components measured on board [30]. When evaluating the Fisher matrix, we consistently perform the analysis at the reference point, where the weights of the spline are zero. In other words, this is the point where the PSD is equal to the reference value as illustrated in Fig. 2.

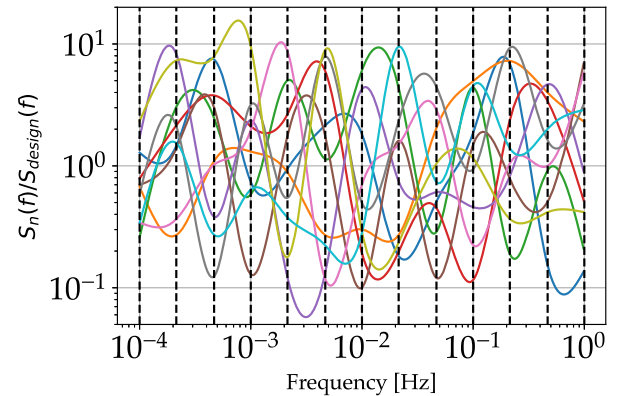


FIG. 1. Deviations from the design power spectral density obtained using the cubic spline model, with  $\lambda_i \sim U[-1, 1]$ , and with knots equally spaced between  $\log_{10}(f) = -4$  and  $\log_{10}(f) = 0$ . The plot shows the ratio of the total PSD and the design one for different parameter realizations  $\lambda_i$ .

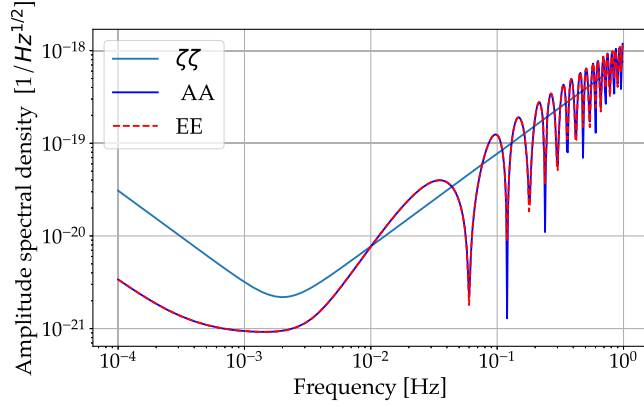


FIG. 2. Reference amplitude spectral density for the time delay interferometry channels  $A$ ,  $E$ , and  $\zeta$  considering only test mass acceleration and optical metrology noise and assuming a constellation of three fixed unequal arm lengths.

Figure 3 illustrates that, in the case of unequal but constant arm length, the CSDs are smaller at low frequencies by between 1 and 3 orders of magnitude when compared to the PSDs shown in Fig. 2. However, this assumes that the TM and OMS noise for each single-link measurement have the same spectral density. It was shown in [11] that, when the LISA response is constructed with unequal values of the six TM and six OMS noise terms, the CSD can be much larger and becomes comparable to the PSD.

We want to adopt a model for the noise that allows for unexpected and unmodeled noise components and for variations in the spectral densities of the TM and OMS noise in each single-link measurement to be unequal. To do so, we cannot use the CSD of three unequal but fixed-length arms with equal TM and OMS noise levels as a reference, as the CSD is unusually suppressed under those

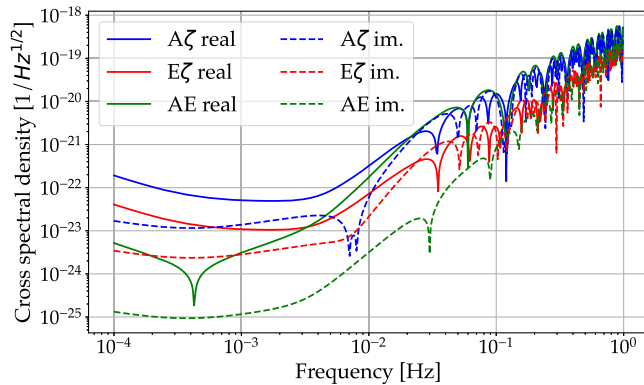


FIG. 3. Real and imaginary part of the reference square root of the cross-spectral density for the time delay interferometry channels  $AE$ ,  $E\zeta$ , and  $A\zeta$  considering only TM acceleration and OMS noise and assuming a constellation of three fixed unequal arm lengths.

assumptions. Instead, we adopt the following model for the CSD<sup>1</sup>:

$$\Re\{S_n(f|\vec{\lambda})\} = \sqrt{S_{\text{des},i}(f)S_{\text{des},j}(f)\sigma_R}10^{C(f|\vec{\lambda})}$$

$$\Im\{S_n(f|\vec{\lambda})\} = \sqrt{S_{\text{des},i}(f)S_{\text{des},j}(f)\sigma_I}10^{C(f|\vec{\lambda})}, \quad (13)$$

where  $\text{Re}$  stands for the real part and  $\text{Im}$  for the imaginary part. The indices  $i$  and  $j$  run over the number of detectors or channels with  $i \neq j$ . We have introduced the factors  $\sigma_I$  and  $\sigma_R$  to scale the amplitude of the CSD relative to the geometric mean of the PSDs.

This model allows for larger CSD variations than those in the case of equal noise terms (as in Fig. 3). This is consistent with the results presented in [11]. We choose the value of  $\sigma_I$  according to Fig. 3 where the imaginary component is about 1–2 orders of magnitude smaller than the real components at low frequencies. The value of  $\sigma_R$  was chosen accordingly to what is reported in [11] in case of unequal TMs and OMS noise terms where the real part of the CSD is 1% of the PSD. Thus, in the analysis we fixed  $\sigma_R = 0.1$  and  $\sigma_I = 0.8\sigma_R$ . For completeness, we have also run several tests changing the value of both factors, and we have observed that varying these choices for  $\sigma_I$  and  $\sigma_R$  does not significantly change the conclusions.

It is important to state that our model is not completely general, since we are imposing a certain amount of smoothness in the PSD variation, and, consequently, in the CSD, when we specify the number and spacing of the knots. Thus, we are not able to fit all possible noise scenarios. In particular, this model does not attempt to reproduce the zeros of the TDI transfer functions faithfully. This will become important above  $f \sim 0.05$  Hz, but this should not affect our results as the SGWBs we consider do not have much power at those frequencies, as can be seen from Fig. 6. Other models could be considered, for example, by imposing the spline variations at the level of the noise in individual laser links (generalizing the approach taken in [25]), before applying the TDI transfer function. This should be explored in the future, but this would increase the number of parameters further so we might expect there to be additional degeneracies, which would lead to practical difficulties in fitting noise and

<sup>1</sup>In principle, our model does not force the matrix to be positive definite. We are forcing the reference spectral density matrix to be positive definite, but, in principle, we could have a factor of 10 variation in the CSD while the PSD is unchanged. It does not matter for the Fisher matrix, because this is a local approximation and we are evaluating it at a point where the matrix is positive definite. The CSD at the central point is 0.1 of its maximum value, so in an open set around that point, it will be positive definite, and, thus, all derivatives are well defined. The conclusion is that the model used here is fair for what we want to demonstrate but would not be a suitable model to use when analyzing the data.

signal simultaneously. However, for the current study, the model we use is adequate to represent generic, slowly varying, fluctuations in the PSD and CSD.

#### D. Noise at the TDI input and outputs

In this section, we will describe the instrumental noise model used to define the reference PSD in this work. The LISA constellation is designed to have three identical spacecraft positioned in a triangular formation, spaced 2.5 million km apart, and interconnected by six active laser links. The orbital configuration aims for an equilateral triangle, but celestial dynamics causes a change of the arm lengths of approximately 1.5% over a year, along with a relative drift of up to 10 m/s between satellites [1]. Consequently, the LISA interferometers experience unequal and time-varying arm lengths, which leads to contamination of the measurement channels by laser frequency noise. To address this, a postprocessing technique known as TDI is applied [31]. TDI involves combining raw phase meter data on the ground by appropriately time shifting them and creating an equivalent interferometer with equal arm lengths that is insensitive to laser frequency noise. The initial formulation of “first-generation TDI” was for a static constellation [17], but “modified first-generation” combinations were later identified in [32]. These combinations consider a rigid rotation of the constellation around its center of mass. Lastly, combinations accounting for relative velocities between spacecraft due to the orbital dynamics of the LISA constellation, termed “second-generation TDI,” were introduced in [33,34].

The standard second-generation TDI channels are the Michelson interferometer channels  $X$ ,  $Y$ , and  $Z$ , from which we form the more GW-sensitive channels  $A$  and  $E$  [35]. Together with the GW-sensitive channels, we consider a null channel, the  $\zeta$  channel [36], that is less sensitive to GWs and can, in principle, be used as a noise monitor.

In the current work, we will assume that laser noise has already been reduced; thus, we can work directly with the first-generation TDI [37]. Indeed, as reported in [22,37], for assessing the interaction of nonsuppressed factors, such as gravitational wave signals and various secondary noise sources, it is usual to use the assumption of first-generation TDI. This choice is justified by the fact that, when our focus is on reducing laser frequency noise (often by orders of magnitude), the impact of slight discrepancies and dynamic alterations in arm lengths becomes significant. However, in the context of mitigating nonsuppressed effects and modeling the instrument response to GWs, these mismatches and changes introduce only small corrections to the corresponding results.

We will also assume that all known calibrated and measured instrumental noise sources have been subtracted, such as the optical tilt-to-length cross-coupling to spacecraft motion and clock noise [19,38,39]. As mentioned earlier, the primary sources of secondary noise, for which

we have neither a measurement for coherent subtraction nor a high-precision *a priori* model [16], are the TM and OMS noise components.

We represent the TM acceleration noise PSD of a single TM by  $S_{g_{ij}}$ . To directly compare the OMS and TM contributions, we can directly convert the acceleration noise of a single TM to an equivalent displacement, whose PSD is given by

$$S_{g_{ij}}^{\text{disp}} = S_{g_{ij}} / (2\pi f)^4, \quad (14)$$

where  $f$  is the Fourier frequency. We denote the time series associated with this displacement as  $x_{ij}^g(t)$ . We also define the PSD of the OMS noise as  $S_{\text{oms}_{ij}}(f)$ , and we denote the time series of the single OMS as  $x_{ij}^m(t)$ . All TDI combinations can be constructed from a combination of single-link TM to TM measurements. Such measurements are represented by the intermediary variables [22]:

$$\tilde{\eta}_{ij}^N(\omega) = \tilde{x}(\omega)_{ji}^g e^{-i\omega L_{ji}} + \tilde{x}(\omega)_{ij}^g + \tilde{x}(\omega)_{ij}^m, \quad (15)$$

where  $\tilde{\eta}_{ij}^N(\omega)$  is the noise in a single-link measurement, the first index  $i$  indicates the spacecraft where the measurement is performed at time  $t$ , the second index  $j$  indicates the distant spacecraft from which light was emitted at time  $t - \tau$ , and  $\omega = 2\pi f$ . Equation (15) implies that each single-link measurement contains TM noise terms from the distant and local spacecraft, such that the TM noise appearing in the measurements on the two ends of the same arm is correlated (between the two links):

$$\langle \tilde{\eta}_{ij}^N(\omega) \tilde{\eta}_{ji}^N(\omega) \rangle \neq 0. \quad (16)$$

From these measurements, it is possible to build any TDI channels [17,40] and, therefore, the corresponding first-generation orthogonal channels  $A_1$  and  $E_1$  [22,35,37] that will be used in this work:

$$A_1 = \frac{Z_1 - X_1}{\sqrt{2}}, \quad E_1 = \frac{X_1 - 2Y_1 + Z_1}{\sqrt{6}}. \quad (17)$$

The  $X_1$  variable is defined as

$$X_1 = (D_{13}D_{31} - 1)(\eta_{12} + D_{12}\eta_{21}) + (1 - D_{12}D_{21})(\eta_{13} + D_{13}\eta_{31}), \quad (18)$$

where the delays  $D_{ij}$  correspond to a constant time shift and, thus, in frequency to  $\mathcal{F}\{D_{ij}\} = e^{-i\omega L_{ij}}$ . The  $Y_1$  and  $Z_1$  are given from  $X_1$  by cyclic permutations of the three satellites. The fully symmetric channel  $\zeta_1$  is defined by

$$\zeta_1 = D_{12}(\eta_{31} - \eta_{32}) + D_{23}(\eta_{12} - \eta_{13}) + D_{31}(\eta_{23} - \eta_{21}). \quad (19)$$

The assumed model for the TM acceleration noise is [27]

$$E\langle \tilde{x}_{ij}^g(f) \tilde{x}_{lm}^{g*}(f') \rangle = \frac{1}{2} \delta_{il} \delta_{jm} \delta(f - f') S_{g_{ij}}(f),$$

$$S_{g_{ij}}(f) = \left( 3 \times 10^{-15} \frac{m}{s^2 \sqrt{\text{Hz}}} \right)^2 \times \left( 1 + \left( \frac{0.4 \text{ mHz}}{f} \right)^2 \right) \left( 1 + \left( \frac{f}{8 \text{ mHz}} \right)^4 \right), \quad (20)$$

and for the OMS noise [27]

$$E\langle \tilde{x}_{ij}^m(f) \tilde{x}_{lm}^{m*}(f') \rangle = \frac{1}{2} \delta_{il} \delta_{jm} \delta(f - f') S_{\text{oms}_{ij}}(f),$$

$$S_{\text{oms}_{ij}}(f) = (15 \text{ pm}/\sqrt{\text{Hz}})^2 \times \left( 1 + \left( \frac{2 \text{ mHz}}{f} \right)^4 \right). \quad (21)$$

This model assumes that individual noise components are uncorrelated. In reality, the test masses in the same satellite will share environmental noise, such as temperature fluctuations, so this assumption might not hold. However, this model serves as a reference one, and any variation is captured by the flexible spline model previously presented.

As the LISA satellite constellation would ideally form an equilateral triangle, we opted to address the arm-length inequality by assuming that LISA experiences a small, static distortion along any of the triangle's normal modes, as described in [36]. Reference [41] examines the impact of these distortion modes and identifies which ones effectively alter LISA in comparison to its nominal state. When considering linear terms in the distortion, only the  $a$  mode,  $b$  mode, and dilation mode ( $d$  mode) contribute to a change in arm lengths. The dilation mode distorts LISA uniformly in all directions, preserving the assumption of equal arm lengths. On the other hand, the  $a$  mode and  $b$  mode introduce a differential change between the arms while maintaining the overall perimeter of the triangle at its nominal value. Consequently, we focus solely on the  $a$  mode and  $b$  mode, assuming these have amplitudes  $\delta_a$  and  $\delta_b$ , while all other modes have zero amplitude.

One can then express the arm lengths  $L_{ij}$  in terms of these modes of the LISA triangle as

$$L_{12}(t) = L \left[ 1 + \frac{1}{2} (\sqrt{3} \delta_a - \delta_b) \right], \quad (22a)$$

$$L_{23}(t) = L(1 + \delta_b), \quad (22b)$$

$$L_{31}(t) = L \left[ 1 - \frac{1}{2} (\sqrt{3} \delta_a + \delta_b) \right]. \quad (22c)$$

The full expressions are rather long; thus, we give them in a separate *Mathematica* notebook file [42], and we plot them in Figs. 2 and 3. The amplitude spectral density (ASD) and CSDs are computed in terms of  $\delta_a$  and  $\delta_b$ . Indeed, while

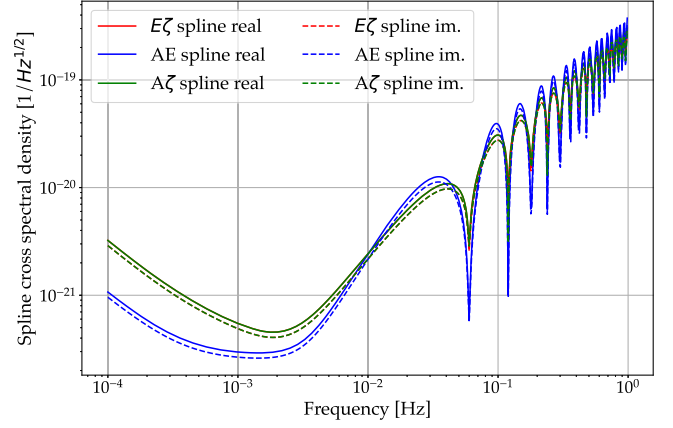


FIG. 4. Real and imaginary part of splines-square root cross-spectral density for the time delay interferometry channels  $AE$ ,  $E\zeta$ , and  $A\zeta$  considering test mass acceleration and optical metrology noise assuming a constellation of three fixed unequal arm lengths. This is the CSD model adopted in the analysis of this paper. The expression can be found in Eq. (13).

$L = (L_{12} + L_{23} + L_{31})/3 \approx 8.3$  s is the average arm length, the small parameters  $\delta_a$  and  $\delta_b$  are typically  $\sim 0.005$ – $0.009$  for realistic ESA orbits<sup>2</sup> [43].

We consider that the six test masses noise terms have the same PSD as well as the six OMS noise terms, but this suppresses the contribution in the CSD as visible in Fig. 3. It was shown in [11] that if the levels of the noise terms differ by 20%, then the CSD can be 10% of the PSD at low frequencies and several tens of percent at high frequency. This motivates the particular choice of flexible CSD model that we introduced in Eq. (13), and it is illustrated in Fig. 4.

### E. Signal transfer function

The detector response to a stochastic background can be computed by expressing a GW signal as a superposition of plane waves and by assuming that the LISA constellation has static arm lengths and it is in a flat background spacetime. Following [11], it is possible to show that the component of the single-link measurement  $\eta_{ij}(t)$  due to a GW is given by

$$\eta_{ij}^{\text{GW}}(t) = i \int_{-\infty}^{\infty} \left\{ \frac{f}{f_{ij}} e^{2\pi i f(t-L_{ij})} \times \int \left[ e^{-2\pi i f \hat{k} \cdot \vec{x}_i} \sum_{\mathcal{A}} \xi_{ij}^{\mathcal{A}}(f, \hat{k}) \tilde{h}_{\mathcal{A}}(f, \hat{k}) \right] d\Omega_{\hat{k}} \right\} df, \quad (23)$$

where  $i$  stands for imaginary component,  $f_{ij} = (2\pi L_{ij})^{-1}$ ,  $\vec{x}_i$  denotes the position of satellite  $i$ ,  $\mathcal{A} = +, \times$  denotes the GW polarization,  $\tilde{h}_{\mathcal{A}}(f, \hat{k})$  is the Fourier transform of the

<sup>2</sup>Note that the case  $\delta_a = \delta_b = 0$  corresponds to the equal-arm LISA scenario. In the paper, we used  $\delta_a = -0.005$  and  $\delta_b = 0.009$ .

GW signal,  $f$  is the GW frequency,  $\hat{k}$  is the outward vector in the direction of the incoming GW, and  $d\Omega_{\hat{k}}$  is the infinitesimal solid angle. The above expression quantifies the fractional frequency shift due to a superposition of plane waves coming from different directions  $\hat{k}$ .

The term  $\xi_{ij}^A$  projects the incoming wave with polarization  $\mathcal{A}$  onto the detector, and its functional dependence is given by

$$\xi_{ij}^A(f, \hat{k}) = e^{-2\pi i f \hat{k} \cdot \vec{L}_{ij}} \mathcal{M}_{ij}(f, \hat{k}) \mathcal{G}^A(\hat{k}, \hat{l}_{ij}), \quad (24)$$

where

$$\mathcal{M}_{ij}(f, \hat{k}) \equiv e^{\pi i f L_{ij}(1 + \hat{k} \cdot \hat{l}_{ij})} \text{sinc}(\pi f L_{ij}(1 + \hat{k} \cdot \hat{l}_{ij})) \quad (25)$$

and

$$\mathcal{G}^A(\hat{k}, \hat{l}_{ij}) \equiv \frac{\hat{l}_{ij}^a \hat{l}_{ij}^b}{2} e_{ab}^A(\hat{k}), \quad (26)$$

where  $\hat{l}_{ij} = (\vec{x}_j - \vec{x}_i)/|\vec{x}_j - \vec{x}_i|$  is a unit vector pointing from spacecraft  $i$  to  $j$  and  $e_{ab}^A(\hat{k})$  denotes the GW polarization tensors.

For a homogeneous, isotropic, and nonchiral, stochastic background, the GW signal is specified only statistically. We assume the SGWB can be described as a Gaussian, homogeneous, isotropic, and nonchiral background [11] with zero mean and second moment given, respectively, by

$$\langle \tilde{h}_A(f, \hat{k}) \tilde{h}_B^*(f', \hat{k}') \rangle = \delta(f - f') \delta(\hat{k} - \hat{k}') \delta_{AB} \frac{P_h^{AB}(f)}{16\pi}$$

and

$$\langle \tilde{h}_A(f, \hat{k}) \tilde{h}_B(f', \hat{k}') \rangle = 0.$$

Homogeneity and isotropy implies that  $P_h^{AB}(f)$  is diagonal, whereas the nonchirality implies  $P_h^{\times\times} = P_h^{++}$ , so that we can define  $P_h := \sum_{\mathcal{A}} P_h^{AA}$ . For a Gaussian background, the second moment completely specifies the distribution. We then characterize the response of the individual links to a stochastic background statistically:

$$\langle \tilde{\eta}_{ij}^{\text{GW}} \tilde{\eta}_{mn}^{\text{GW}} \rangle = \frac{1}{2} S_{ij,mn}^{\eta, \text{GW}}(f) \delta(f - f'), \quad (27)$$

where spectral densities for the link measurements are given by

$$S_{ij,mn}^{\eta, \text{GW}}(f) = \frac{f^2}{f_{ij} f_{mn}} e^{-2\pi i f (L_{ij} - L_{mn})} \sum_{\mathcal{A}} P_h^{AA}(f) \Upsilon_{ij,mn}^{\mathcal{A}}(f), \quad (28)$$

with

$$\Upsilon_{ij,mn}^{\mathcal{A}}(f) = \int \frac{d\Omega_{\hat{k}}}{4\pi} e^{-2\pi i f \hat{k} \cdot (\vec{x}_i - \vec{x}_m)} \xi_{ij}^{\mathcal{A}}(f, \hat{k}) \xi_{mn}^{\mathcal{A}}(f, \hat{k})^*. \quad (29)$$

The power spectral densities of the signal in the TDI variables described in Sec. II D can then be computed from

$$\begin{aligned} \langle \tilde{U}(f) \tilde{V}^*(f') \rangle &= \frac{1}{2} S_{\text{UV}}^{\text{GW}}(f) \delta(f - f'), \\ S_{\text{UV}}^{\text{GW}}(f) &= \sum_{ij,mn \in \mathcal{I}} c_{ij}^U(f) c_{mn}^{V*}(f) S_{ij,mn}^{\eta, \text{GW}}(f), \end{aligned} \quad (30)$$

where  $\tilde{U}$  and  $\tilde{V}$  denote any two TDI variables, which in our case are TDI  $A$ ,  $E$ , and  $\zeta$ , and  $\mathcal{I} = \{12, 13, 23, 21, 31, 32\}$  denotes the set of pairs of indices that define the six intersatellite links. The coefficients  $c_{ij/mn}^U$  map the single-link measurements onto the TDI variable  $U$ . Refer to the *Mathematica* code for the computation of such coefficients [42].

Note that, considering each polarization of the SGWB contributes equally to the background, i.e.,  $P_h^{\times\times} = P_h^{++}$ , we can rewrite Eq. (30) as a product of the SGWB spectral density  $P_h(f)$  and a transfer function  $\mathcal{T}^{\text{GW}}(f)$  which takes into account the LISA detector response, i.e.,  $S_{\text{UV}}^{\text{GW}}(f) = \mathcal{T}^{\text{GW}}(f) P_h(f)$ .

$S_{\text{UV}}^{\text{GW}}(f)$  would correspond to the first term on the right-hand side of Eq. (5). The transfer functions for the three TDI channels and their cross-correlation are shown in Fig. 5.

## F. SGWB signal models

There is a large variety of models for SGWBs that might manifest in the LISA band [44]. In this work, we focus on four models, which can be described by their energy density  $h^2 \Omega_{\text{GW}}$  [45], which is a function of some parameters  $\theta$  that vary depending on the model considered. The fiducial parameters of the models are chosen to be compatible with either physical phenomena or with direct observational constraints from LIGO-VIRGO-KAGRA. They are also chosen so that the signals are in the LISA band, with the pivot frequency fixed to be in the middle of the log-frequency range. This is an arbitrary choice, but it is made so that the amplitude at this frequency is representative of the amplitude of the background where LISA is most sensitive. In the first part of our analysis, we will vary the amplitude to assess the degradation in the precision of parameter estimation when including noise knowledge uncertainty, across the full range of background models. In the second part of our analysis, we will choose a fixed value of the amplitude based on the SNR such that, given the same SNR for all the models considered, we can quantify what is the prior noise knowledge that we would need to be able to estimate a certain model with sufficient

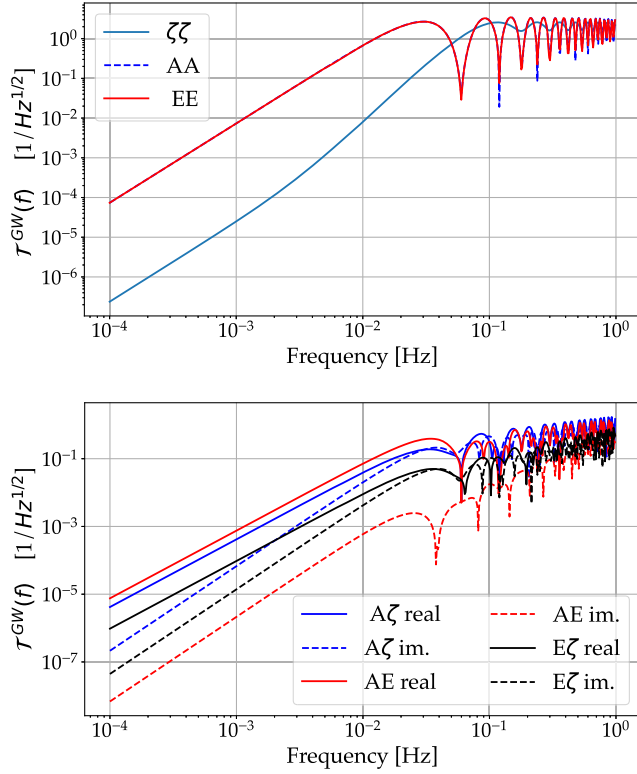


FIG. 5. Upper panel: gravitational wave transfer functions  $\mathcal{T}^{\text{GW}}(f)$  of the three time delay interferometry channels  $A$ ,  $E$ , and  $\zeta$  assuming a constellation of three fixed unequal arm lengths; lower panel: real and imaginary components of the gravitational wave transfer functions  $\mathcal{T}^{\text{GW}}(f)$  of the time delay interferometry channels  $AE$ ,  $E\zeta$ , and  $A\zeta$ .

precision. Nonetheless, we include reference values for the amplitude to make a link to models described in the literature. The notebook that we have used for running all the analyses is available in [42] and can, therefore, be tuned by the user for other research projects.

The four models used in our analysis are the following.

(i) *Power law.*

$$h^2\Omega_{\text{GW}}(f) \approx A \left( \frac{f}{f_p} \right)^n, \quad (31)$$

where  $f_p$  is the pivot frequency, defined as the geometrical mean of the LISA frequency interval ( $10^{-4}$  Hz, 0.1 Hz),  $f_p = 3$  mHz. The model parameters are the log amplitude  $A$  and slope  $n$  [46,47]. We use reference values of  $n=2/3$  and  $A=7.87 \times 10^{-13}$ , representing a SGWB from stellar-origin black hole binaries that have energy density at 1 mHz of  $h^2\Omega_{\text{GW}}(1\text{mHz})=3.78 \times 10^{-13}$ . This value was chosen to be compatible with LIGO-VIRGO-KAGRA constraints [46].

(ii) *Gaussian bump.*

$$h^2\Omega_{\text{GW}} = A e^{-\frac{1}{2\sigma^2} \ln(\frac{f}{f_p})^2}, \quad (32)$$

where  $f_p$  is the pivot frequency as before. The model parameters are the log amplitude  $A$  and width  $\sigma$ . We use reference values of  $A=10^{-12.48}$  and  $\sigma=0.3$  whose energy density at 1 mHz is  $h^2\Omega_{\text{GW}}(1\text{mHz})=4.05 \times 10^{-16}$ . This signal is chosen as a simple way to mimic the one that might arise from particle production taking place for a limited number of  $e$ -folds during inflation (as, for instance, required by some models of primordial black hole generation) (see, e.g., [48–50]).

(iii) *Power law with running.*

$$h^2\Omega_{\text{GW}} = A \left( \frac{f}{f_p} \right)^{n+\alpha \ln(\frac{f}{f_p})}, \quad (33)$$

where  $f_p$  is the pivot frequency as before. The model parameters are the log amplitude  $A$  the slope  $n$ , and the running index  $\alpha$ . We use reference values of  $A=10^{-12.65}$ ,  $n=1$ , and  $\alpha=-0.1$ . This signal is motivated by nonstandard inflationary models. For example, gravitational wave generation can be enhanced by sustained particle production during inflation, leading to a power law stochastic GW background, which would deviate from a simple power law at a higher frequency when backreaction kicks in (see, e.g., [51]). The energy density at 1 mHz is  $h^2\Omega_{\text{GW}}(1\text{mHz})=6.61 \times 10^{-14}$ .

(iv) *First-order phase transition (FOPT).*

$$h^2\Omega_{\text{GW}}(f) = h^2\Omega_p \left( \frac{f}{f_p} \right)^3 \left( \frac{7}{4 + 3(\frac{f}{f_p})^2} \right)^n, \quad (34)$$

where  $f = 2 \times 10^{-4}$  Hz (note this is different from the reference frequency in the previous models). The model parameters are the energy density  $h^2\Omega_p$  and spectral index  $n$ . We use reference values of  $A \equiv h^2\Omega_p = 10^{-10}$  and  $n=7/2$  whose energy density at 1 mHz is  $h^2\Omega_{\text{GW}}(1\text{mHz})=2.59 \times 10^{-12}$ . This signal is motivated by the production of sound waves in the cosmic fluid from colliding phase transition bubbles [52,53].

In our analysis, we also include the contribution to the spectral density from the foreground of GBs.

We use the following model for the foreground [44].

(i) *Foreground of galactic binaries.*

$$S_{GB}(f) = A_{GB} \left( \frac{f}{\text{Hz}} \right)^{-\frac{7}{3}} e^{-(f/f_1)^\alpha} \times \frac{1}{2} \left[ 1 + \tanh \left( \frac{f_{\text{knee}} - f}{f_2} \right) \right] \quad (35)$$

with

$$f_1 = 10^{a_1 \log_{10}(T) + b_1}, \quad f_{\text{knee}} = 10^{a_k \log_{10}(T) + b_k}$$

setting  $A = 1.15 \times 10^{-44}$ ;  $\alpha = 1.56$ ;  $a_1 = -0.15$ ;  $b_1 = -2.72$ ;  $a_k = -0.37$ ;  $b_k = -2.49$ ;  $f_2 = 6.7 \times 10^{-4}$  Hz; and  $T$  is the observation time. In reality, the foreground of galactic binaries cannot be considered a stationary and isotropic background. The reason is that this background is generated by an ensemble of binaries that are preferentially distributed along the galactic plane. It is not stationary, because LISA moves with respect to the Galactic Center. For simplicity, we treat the galactic binary foreground as stationary and isotropic here so that it can be included on the same footing as the other backgrounds. We set the background amplitude to a value averaged over a year [54]. The time dependence provides additional information to distinguish the galactic background from other backgrounds, so we expect this approach to be conservative, in the sense that it will overestimate the amount of confusion. When considering the background in conjunction with other SGWBs, we allow the amplitude to vary but keep the other parameters fixed.

The relation between the energy density  $\Omega_{\text{GW}}$  and the stochastic GW background power spectral density  $P_h(f)$  is given by [45]

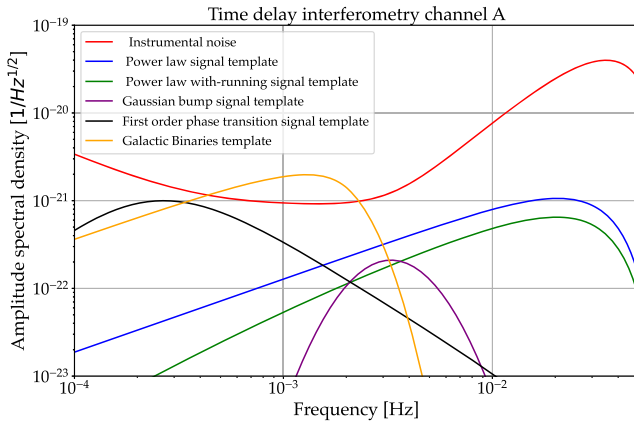


FIG. 6. Amplitude spectral density of the stochastic GW background models and the amplitude spectral density of the reference test mass and optical metrology noise in the time delay interferometry channel A.

TABLE I. Signal-to-noise ratio in TDI channel A for the four SGWB models, with and without the presence of the galactic foreground as an additional noise component. The galactic foreground here is considered to have an SNR of 1627.39.

SGWB model	SNR w/o GB	SNR w/ GB
Power law with running	14.54	13.35
Power law	48.70	42.89
Gaussian bump	13.51	11.65
First-order phase transition	118.68	64.18

$$\Omega_{\text{GW}}(f) = \frac{4\pi^2}{3H_0^2} f^3 P_h(f), \quad (36)$$

where  $H_0$  is the Hubble constant fixed to be 67.8 km/s/Mpc; as a consequence,  $h = 0.678$ . The conversion between the energy density  $\Omega_{\text{GW}}(f)$  and gravitational power spectral density  $P_h(f)$  used to compute Eq. (30) is then [45]

$$P_h(f) = 7.98 \times 10^{-37} \left( \frac{\text{Hz}}{f} \right)^3 h^2 \Omega_{\text{GW}}(f) \frac{1}{\text{Hz}}. \quad (37)$$

We report in Fig. 6 the ASD of the four SGWB models together with the ASD of the reference instrumental noise in TDI channel A [27].

We also provide the computation of the SNRs of these different backgrounds in the TDI channel A using the following formula [55]:

$$\text{SNR}_A = \sqrt{T} \left[ \int_0^\infty \frac{S_{AA}^{\text{GW}}(f)^2}{S_n^A(f)^2} df \right]^{1/2} \quad (38)$$

with an observation period of  $T = 4$  yr. Here  $S_{AA}^{\text{GW}}(f)$  is the spectral density in channel A that can be computed from Eq. (30), and  $S_n^A$  is the PSD of the A channel. The results<sup>3</sup> are shown in Table I.

It is possible to notice that including the foreground as part of the noise [ $S_n^A(f) := S_{GB}^A(f) + S_n^A(f)$ ] leads to a substantial decrease of the SNR for the FOPT background, but the SNR does not change very much for the other models.

We plot in Fig. 7 the value of the SNR in channel A versus the energy density at 1 mHz for the different models. The dotted lines assume no presence of the foreground, whereas the continuous lines include the presence of the foreground. As expected, there is a direct correlation between increasing the energy density and an increase in the SNR. Moreover, the presence of the foreground mostly

<sup>3</sup>We note that this formula is derived assuming that we have access to two independent channels that have uncorrelated noise and perfectly correlated signals. This is not a good approximation to LISA, so the SNR is not directly interpretable. However, it still indicates the relative detectability of different backgrounds.

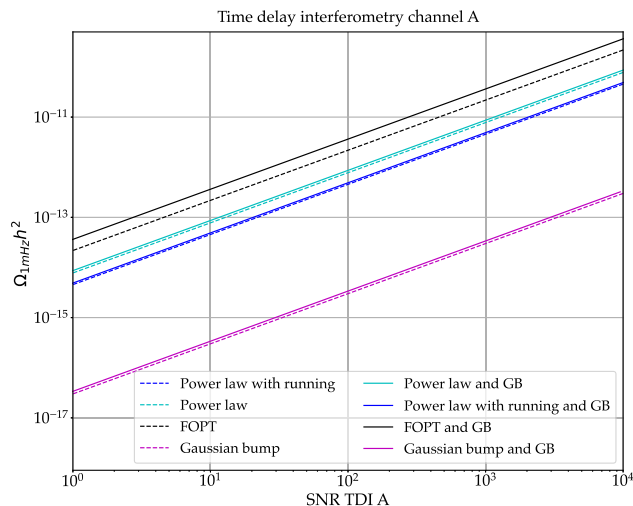


FIG. 7. Signal-to-noise ratio of four different SGWB signals in the TDI channel A, power law, power law with running, Gaussian bump, and first-order phase transition, versus the energy density at 1 mHz, both considering (continuous lines) or not (dashed lines) the presence foreground.

affects the SNR of the FOPT. In fact, in the presence of the foreground, the energy density must be 2 times larger to have the same SNR as it would in the absence of a foreground.

### III. RESULTS

#### A. Impact of instrumental noise knowledge uncertainty on SGWB recovery

Here, we explore how the measurement precision of the SGWB parameters changes in the presence of instrumental noise knowledge uncertainty, for each of the SGWB models described in Sec. II F. We use the Fisher matrix formalism described in Sec. II B, which assumes that the noise is uncorrelated at different frequencies. We assume we use three TDI channels in our analysis,  $A$ ,  $E$ , and  $\zeta$ , as described in Sec. II D. We model uncertainties in the PSD and CSD at each frequency following the model described in Sec. II C. To build the Fisher matrix, we need the following elements:

- (1) The derivatives of the PSD and CSD at each frequency with respect to the parameters of the SGWB model;
- (2) The derivatives of the PSD and CSD at each frequency with respect to the parameter (amplitude) of the galactic binaries—the addition of this parameter extends the dimension of the Fisher matrix by one;
- (3) The derivatives of the PSD and CSD at each frequency with respect to the parameters of the instrumental noise model—the instrumental noise model is based on nine different splines: three splines to model the PSD of  $A$ ,  $E$ , and  $\zeta$  and three

splines each for real and imaginary parts of the CSDs for  $AE$ ,  $A\zeta$ , and  $E\zeta$ . Each spline has several parameters equal to the number of knots, which we take to be 13. The total number of noise parameters is, therefore,  $9 \times 13 = 117$ ;

- (4) The evaluation of the Fisher matrix from these elements using Eq. (8), which is summed over frequency;
- (5) The choice of a prior on the instrumental noise parameters—we use a Gaussian prior, which is implemented in the Fisher matrix formalism by adding the prior matrix to the Fisher matrix before computing its inverse [see Eq. (10)]. For this first study, we take the priors on each noise parameter to be independent, with zero mean and equal variance,  $\sigma_{\text{inst}}$ . In this section, we fix  $\log_{10}(\sigma_{\text{inst}}) = 1$ , which means we are allowing for up to an order of magnitude uncertainty in the instrumental noise at each frequency.
- (6) We compute the inverse of the Fisher matrix after adding the prior to obtain an estimate of the measurement uncertainty, from the square root of the diagonal elements of the inverse as explained in Sec. II B. We also compute the inverse of the SGWB-parameter-only submatrix of the Fisher matrix, which represents the expected uncertainty in the absence of instrumental noise uncertainties.

For each SGWB model, we will present the results in two different ways. First, we will show the ratio of the uncertainties in the SGWB parameters in the presence of instrumental noise uncertainties to those uncertainties when perfect knowledge of the instrumental noise is assumed. These results illustrate the impact of a lack of noise knowledge on SGWB characterization. Second, we will show the actual uncertainties in the SGWB parameters, as computed from the Fisher matrix. Of particular interest is the uncertainty in the log-energy density of the background.

The criterion that we will use as a rule of thumb to determine if a background is detectable will be that  $\Delta \ln(A) \equiv (\Delta A)/A < 1$ . This is a generic criterion that states that the uncertainty in the background amplitude is smaller than the amplitude. As we expect the posterior to be peaked close to the true amplitude and have a width comparable to the measurement uncertainty, this condition states that the posterior on the amplitude peaks significantly far from 0, and so zero amplitude would be ruled out with high confidence. In an analysis of real data, other techniques would be used, such as computing the Bayesian odds ratio for a model including the background to one without. For this study, we need a quick way to evaluate detectability, so we use this criterion which requires only the computation of the Fisher matrix. Making a Gaussian approximation to the likelihood, it can be seen that high Bayesian odds are equivalent to  $\Delta \ln(A) < 1$ , up to factors, and so our conclusions should be robust.

Our results will be presented as a function of the background amplitude (the background energy density) at a reference frequency of 1 mHz [the logarithm of these quantities are linearly related, so they can be easily represented using bottom (top) axes in a single figure]. For the second type of plot, solid lines show results in the presence of noise knowledge uncertainty, and dashed lines give results assuming perfect noise knowledge. In both analyses, we consider the foreground amplitude to vary, and we consider it as an additional source of noise together with the instrumental noise. The upcoming analysis is then computed considering the presence of the Galactic foreground; instead, in Appendix C, we report similar results, computed without taking into consideration the Galactic foreground.

### 1. Power law

A power law SGWB is described by two parameters: the slope and the amplitude. The full Fisher matrix, including instrumental noise and foreground parameters, is  $120 \times 120$ .

Figure 8 shows the results computed for this model. We see that, in the presence of instrumental noise uncertainties, the uncertainty in the SGWB parameters increases by a factor of  $\sim 55$ – $60$ , with the uncertainty in the slope being slightly more affected than that of the amplitude. The increase is lower for high background amplitudes, as expected, but only when the background is 1–2 orders of magnitude brighter than the reference value. Considering the raw uncertainties, we see that the uncertainty in the log-energy density is typically a factor of  $\sim 50$  larger and the background energy density would have to be a factor of  $\sim 50$  times higher to be characterized with the same measurement precision when there is instrumental noise uncertainty as it could be without those uncertainties. However, a background with amplitude equal to the reference value, which has the SNR listed in Table I, should (just) be detectable even allowing for confusion with instrumental noise mismodeling.

### 2. Power law with running

For the power law with running SGWB, the fisher matrix is  $121 \times 121$ , as the SGWB model depends on three parameters: slope, amplitude, and running index  $\alpha$ . The results for this model are shown in Fig. 9. In this case, we see that the uncertainties in the SGWB parameters increase by a factor of  $\sim 30$ – $75$ , with the uncertainty on the amplitude being most affected in this case. Once again, the relative increase in the uncertainty is somewhat lower at higher background amplitudes. The lower panel in Fig. 9 shows that the background is not detectable at the reference amplitude, which has the SNR listed in Table I. An energy density  $\sim 20$  times higher would be required for detection. In general, the background has to have an energy density  $\sim 60$  times higher to be characterized with the same measurement precision when there is instrumental noise

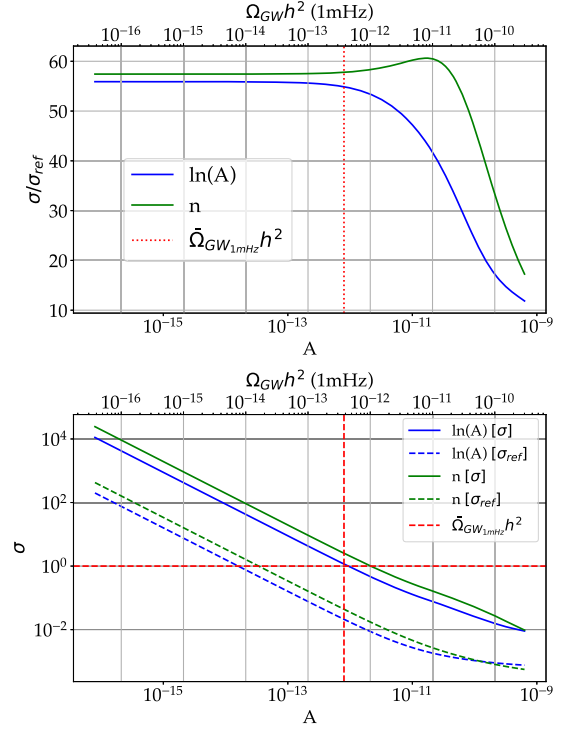


FIG. 8. Results for the power law SGWB model considering the foreground as an additional source of noise. The upper panel shows the ratio of the uncertainties of the SGWB parameters (amplitude and slope) when including instrumental noise uncertainties or assuming perfect noise knowledge. This ratio is plotted versus the amplitude (bottom axis) and SGWB energy density at 1 mHz (top axis). The lower panel shows the estimated parameter uncertainties for the two cases. Once again this is as a function of amplitude or energy density, but for a restricted range. The horizontal red dashed line corresponds to an uncertainty of one, which is our threshold on the uncertainty in log-energy density for deciding that a background is detectable. The vertical red dashed line indicates the reference SGWB amplitude given in Sec. II F.

uncertainty as it could be without those uncertainties, and there is a similar increase in the parameter measurement uncertainty at fixed background energy density.

### 3. Gaussian bump

As for the power law, the Fisher matrix is  $120 \times 120$  as we have two signal parameters: the Gaussian width and the amplitude. The results for this model are shown in Fig. 10. In this case, the degradation in the precision of parameter measurement is a factor of  $\sim 2$ – $8$  when allowing for a lack of knowledge of the instrumental noise. This difference in behavior is related to the different shapes of the SGWBs being considered. A Gaussian is more distinct from the spline model being used to represent the instrumental noise uncertainties than a power law, and, hence, the degree of confusion between the two models is less in this case. From the lower panel in Fig. 10, we see that the energy density in

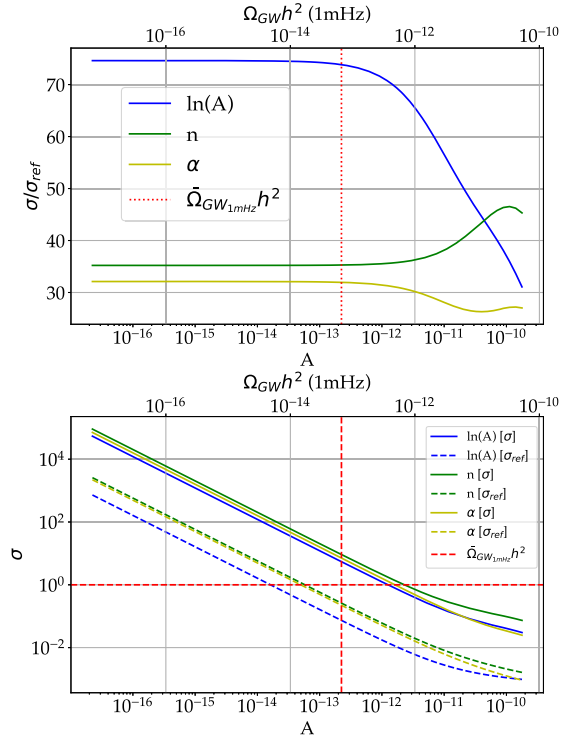


FIG. 9. As in Fig. 8, but now for the power law with running SGWB model.

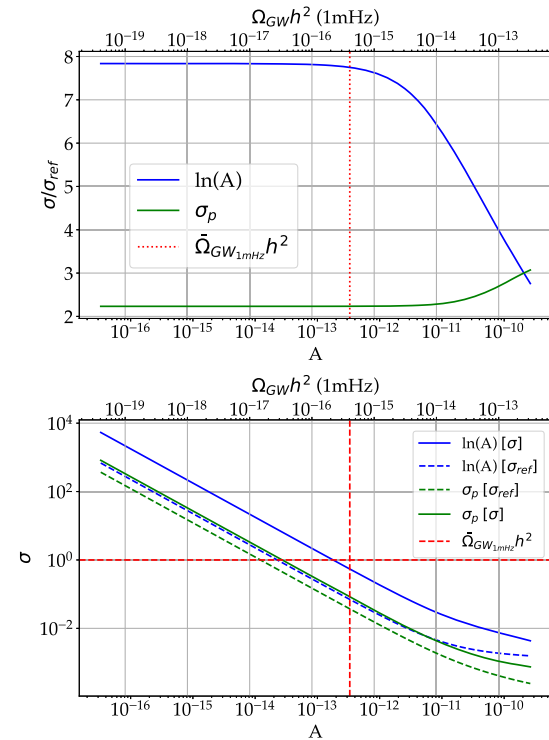


FIG. 10. As in Fig. 8, but now for the Gaussian bump SGWB model.

a Gaussian bump SGWB has to be a factor of  $\sim 10$  times higher for it to be characterized with the same measurement precision when there is instrumental noise uncertainty as it could be in the absence of those uncertainties. A Gaussian bump background at the reference amplitude, which has the SNR listed in Table I, would be detectable; and the width of such a Gaussian could be measured to a few tens of percent precision. This measurement precision improves approximately linearly with the background energy density.

#### 4. First-order phase transition

The FOPT model is again characterized by two parameters, an amplitude and a spectral index, and has a  $120 \times 120$  Fisher matrix. The results for this model are shown in Fig. 11. When allowing for instrumental noise knowledge uncertainties, the precision with which the SGWB log-energy density can be characterized degrades by a factor of  $\sim 20$ . The degradation in the determination of the spectral index is even larger,  $\sim 35$ . Once again, to achieve the same measurement precision, the background energy density would have to be  $\sim 20$  times larger than it would need to be in the absence of noise knowledge uncertainties. Nonetheless, a FOPT background at the reference amplitude, which has the SNR listed in Table I, would still be detectable and provide a measurement of the spectral index at the level of  $\sim \pm 0.8$ .

The previous findings were derived while accounting for the presence of the Galactic foreground. Redoing these

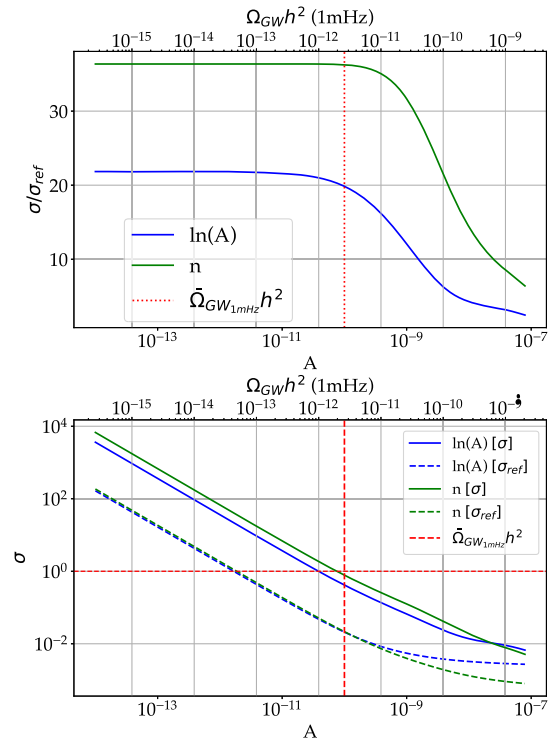


FIG. 11. As in Fig. 8, but now for the first-order phase transition SGWB model.

analyses ignoring the foreground, we do not see big differences in the uncertainty ratio nor in the absolute uncertainties, when these are compared at fixed SNR, i.e., when the signal-to-noise ratio is recomputed without the Galactic binaries included in the spectral density. To illustrate this, we show in Fig. 12 the precision of the measurement of the log-energy density of the background, as a function of the SNR in TDI channel A for all SGWB models, and both including and not including the Galactic binary foreground. We see that the uncertainty is typically larger when the foreground is present, but this is typically less than a factor of a few. The Gaussian bump and power law background are most affected. The uncertainty at fixed SNR and the SNR required for detection both decrease by a factor of a few when the Galactic binary background is removed from the spectral density. For the Gaussian bump, the uncertainty decreases by a factor of a little more than 2 when the Galactic background is excluded. Moreover, the SNR needed to reach the  $\Delta \ln(A) < 1$  threshold for detection decreases by a similar factor. For the power law, the uncertainty decreases by about a factor of 4, and the  $\Delta \ln(A) < 1$  threshold required for detection is reached at an SNR that is a factor of  $\sim 4$  smaller. For the power law with running and the FOPT backgrounds, the uncertainty at fixed SNR is almost unchanged, and the threshold SNR for detection is within a factor of 1.5 and 2, respectively.

This behavior can be understood by looking at the shapes of the various SGWBs in Fig. 6. Figure 7 demonstrates that the removal of the foreground does not affect the SNR very much. The only SGWB that shows a significant change is the FOPT, for which most of the power is at frequencies where the foreground is significant. However, in the region around 300  $\mu\text{Hz}$ , where the majority of the SNR is generated, the shape of the FOPT is very different from the foreground. This is also true for the power law with a

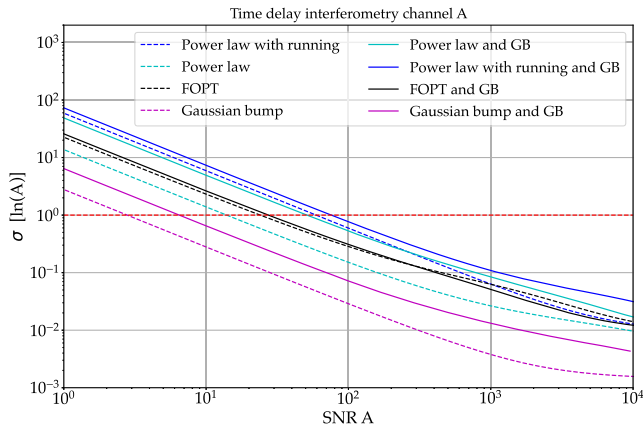


FIG. 12. Signal-to-noise ratio of four different SGWB signals in the TDI channel A, power law, power law with running, Gaussian bump, and first-order phase transition versus the error in log amplitude both considering (continuous lines) or not (dashed lines) the presence foreground.

running model around 5 mHz, where the majority of its SNR is generated. The power law model, on the other hand, is quite parallel to the foreground at low frequency, and the Gaussian bump is quite parallel to the foreground at a few millihertz. This most likely explains why the latter two backgrounds are more difficult to distinguish from a Galactic foreground and, therefore, more affected by its inclusion.

## B. Setting a noise knowledge requirement

In this section, we will explore how the amount of uncertainty in the instrumental noise impacts the results. In practice, we will not be completely ignorant of the instrumental noise. Measurements on board the satellites will indicate the size of certain noise components. In principle, it might therefore be possible to place a requirement on how well the instrumental noise must be known to not degrade the science output of the mission. To assess this, we will recompute the results while changing the variance of the Gaussian prior to the instrumental noise spline parameters. We will vary the prior on the spline weights from very small values [ $\log_{10}(\sigma_{\text{inst}}) = -10$ ], representing near-perfect knowledge of the noise, to very high values  $\log_{10}(\sigma_{\text{inst}}) = 6$ , representing no knowledge of the noise.

We fix the amplitude of the background for each SGWB model so that it corresponds to an SNR of  $\sim 120$ – $142$  in each case: 135 for the power law with running, 138 for the power law, 142 for the first-order phase transition, and 120 for the Gaussian bump. This choice of SNR was motivated by Fig. 12, which shows that an SNR greater than 100 is required to ensure all types of SGWB are detectable. For the case of the power law, we also show results with the amplitude set to the reference energy density, which shows that the exact choice of background amplitude does not make a significant difference to the qualitative behavior, only to the absolute value of the uncertainty.

For all SGWB models, we again present the results in two different ways: as a ratio of the SGWB parameter measurement uncertainties when instrumental noise uncertainties are considered to those assuming perfect noise knowledge and as the absolute measurement uncertainty. Results for the power law model are shown in Fig. 13, for the power law with running model in Fig. 14, for the Gaussian bump model in Fig. 15, and for the FOPT in Fig. 16.

The results for all four SGWB models are qualitatively similar. For very low prior uncertainties, the ratio of the uncertainties tends to be unity. This is expected, as this limit corresponds to the limit in which the instrumental noise is perfectly known. As the prior uncertainty is increased beyond  $\sim 10^{-6}$ , the measurement precision in the presence of noise knowledge uncertainties starts to increase. When the noise knowledge uncertainty reaches  $\sim 10^{-2}$  for power law and Gaussian bump,  $\sim 10^{-1}$  for power law with

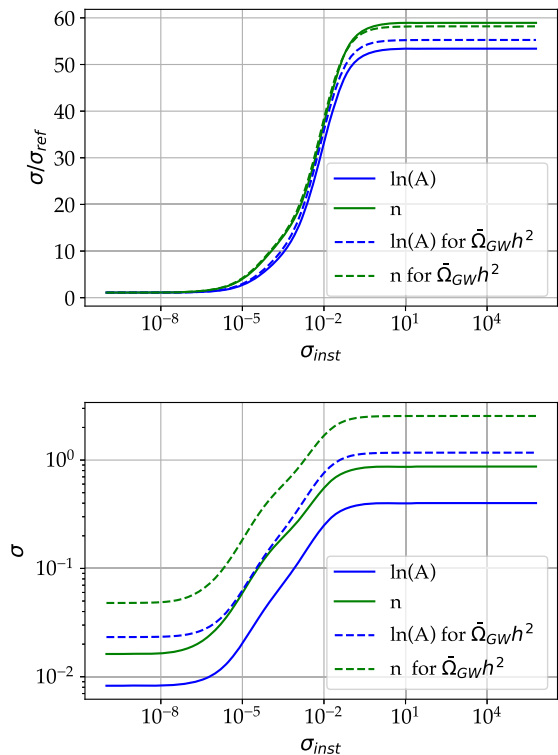


FIG. 13. As in Fig. 8, but now for fixed background amplitude and varying the variance of the Gaussian prior on the instrumental noise spline model. This plot is for a power law background, and the amplitude has been fixed such that the SNR in TDI channel A is 138 (continuous line) and 42.89 (dashed lines).

running, and 10 for FOPT, the measurement precision ratio saturates. This final value reflects the expected uncertainty in the absence of any noise knowledge. The results given in Sec. III A were all computed in this regime.

The main conclusion from these results is that if we wanted to ensure that there was no degradation in LISA science due to lack of noise knowledge, the requirement on the noise knowledge would be  $\ll 10\%$ .

In the LISA Pathfinder mission, which was designed to accurately characterize the free-fall performance of test masses in a space-based environment, the observed noise could be explained only within some margin: The physical origin of the measured submillihertz acceleration is only partially understood, as more than 50% of its PSD is still unmodeled [28,56].

It is therefore unrealistic to expect that a noise requirement at the  $\sim 1\%$ – $10\%$  level could be met. At noise uncertainties above this threshold, there is little difference between some and no noise knowledge, at least within the model for instrumental noise variations considered here. We conclude that no useful and achievable noise knowledge requirement could be implemented in practice.

While we will not be able to achieve the precision that would be possible under ideal circumstances, it is important to emphasize that this does not mean we will not be able to

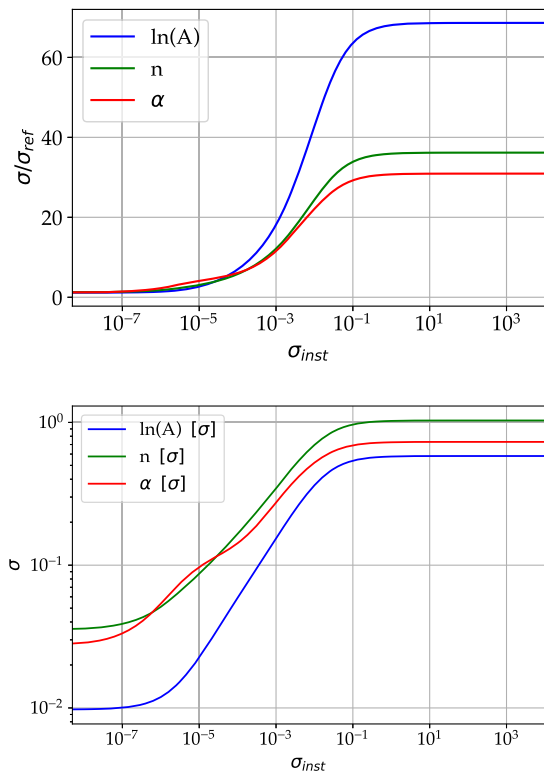


FIG. 14. As in Fig. 13 but now for the power law with running model. The background amplitude has been fixed to give an overall SNR of 135.

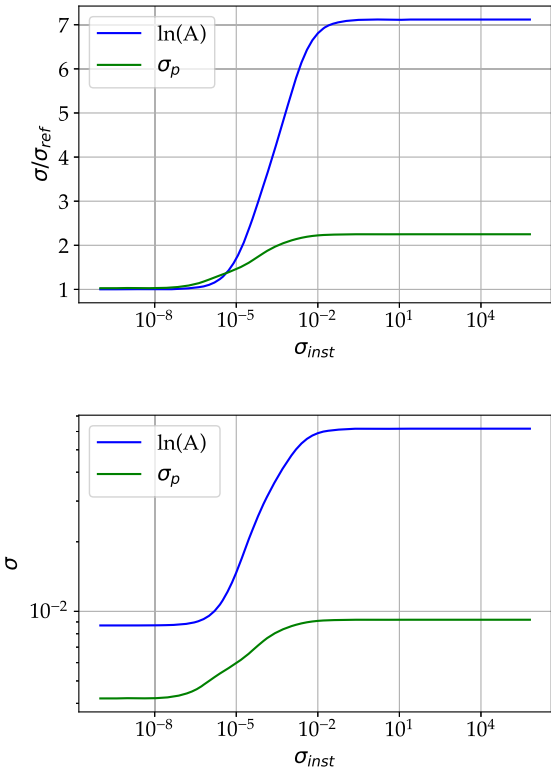


FIG. 15. As in Fig. 13 but now for the Gaussian bump model. The background amplitude has been fixed to give an overall SNR of 120.

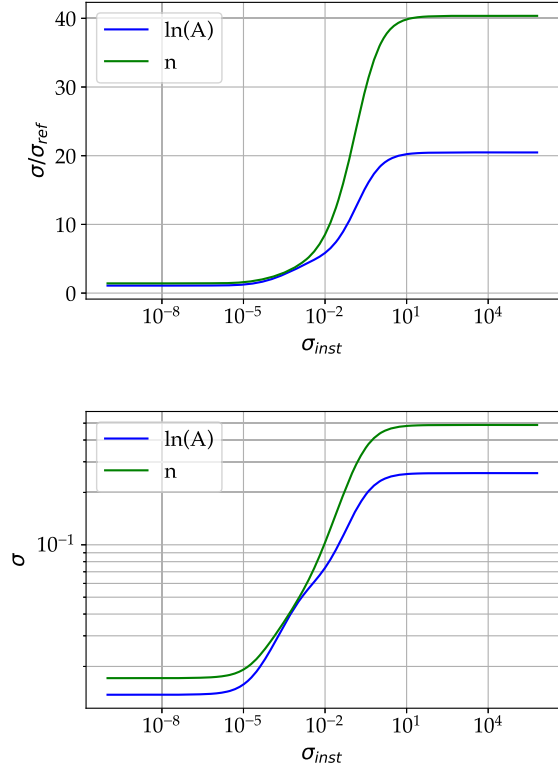


FIG. 16. As in Fig. 13 but now for the FOPT model. The background amplitude has been fixed to give an overall SNR of 142.

detect and characterize modeled SGWBs. In all cases, at SNR of  $\gtrsim 100$ , the amplitude can be constrained to a few tens of percent, even without any knowledge of the instrumental noise.

### C. Signal reconstruction

To finish this section, we will use our Fisher matrix results to illustrate how well we can reconstruct the power law, the foreground, and the instrumental noise. To do this, we will approximate the posterior distribution on the model parameters using a multivariate Gaussian with a covariance matrix equal to the inverse of the Fisher matrix. We can then take random draws from this fake<sup>4</sup> posterior distribution and plot the PSD of the SGWB, the foreground, and instrumental noise corresponding to the drawn parameters. In Fig. 17, we follow this procedure for a power law signal with an SNR of 138 as in the previous section. In Appendix C 5, we report the results for the reconstruction of a power law signal with SNRs of 48 and 971 to illustrate the impact of a smaller and bigger amplitude, respectively, on the results.

<sup>4</sup>Even if the measurements  $x$  are Gaussian, the posterior is not, because it is a function of  $\theta$ . A Gaussian with unknown variance  $\sigma$  is not a Gaussian on that variance;  $p(x|\theta) \propto \frac{1}{\sigma} \exp(-\frac{x^2}{2\sigma^2})$  is a Gaussian in  $x$  but not in  $\sigma$ .

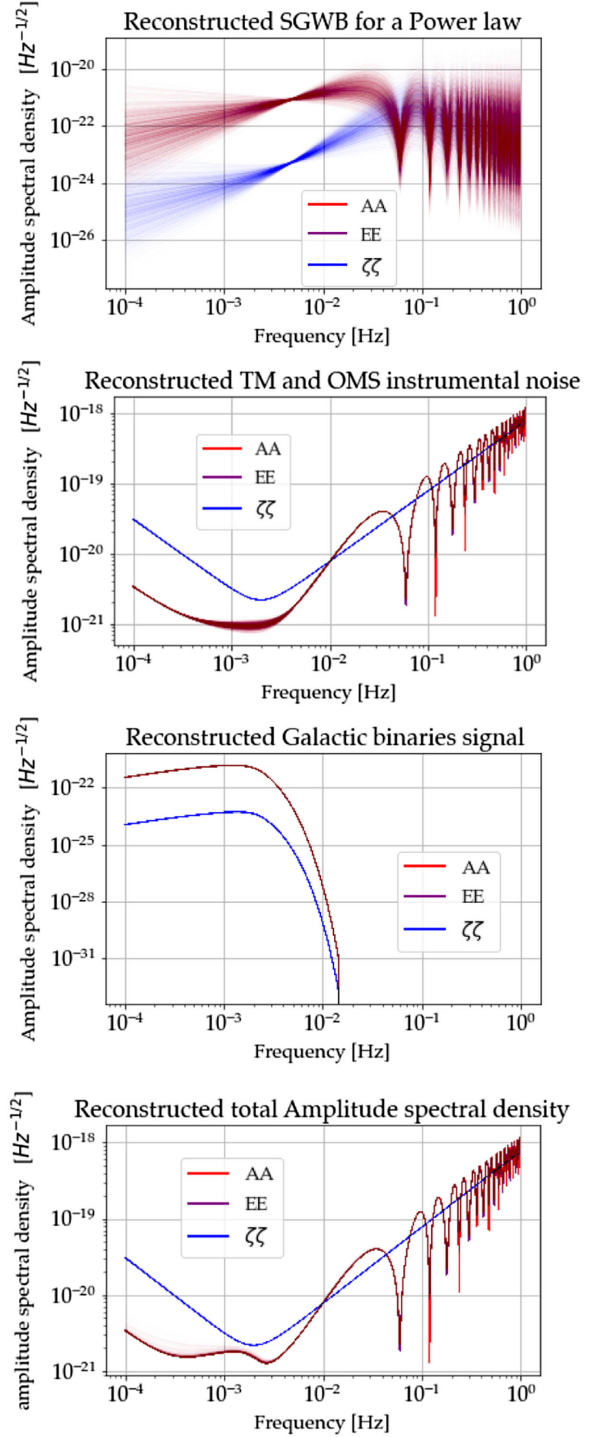


FIG. 17. We show the power law signal, noise ASDs, and Galactic binaries corresponding to random draws from the posterior, approximated using the Fisher matrix as described in the text. In each panel, the curves correspond to the three TDI channels:  $A$  (red),  $E$  (purple), and  $\zeta$  (blue). The upper first panel: reconstructed SGWB; the upper second panel: reconstructed TM and OMS instrumental noise; the middle panel: reconstructed Galactic binaries; the lower panel: total reconstructed ASD (signal + noise + GB). Note that the TDI combinations  $A$  and  $E$  are overlapping.

The four panels show the reconstructed ASDs for the power law, for the foreground, and for the instrumental noise and the total, which is the sum of the three.

What we would expect is that our ability to measure the total spectral density is roughly independent of the relative amplitudes of the two components, since this is what we see and measure in the data. Our model attempts to split that measurement into constituent components. If one of those components is much weaker than the other, we would not expect to recover it as well as when the components are making comparable contributions to the data. Figure 17 is consistent with this expectation, as it shows the Galactic binaries are well recovered in comparison with the power law signal or the noise, both of which show more uncertainty. Moreover, the noise-only reconstruction for the TDI *A* and *E* suffers from the presence of the GW background and foreground in the regime 0.4–4 mHz, where these two signals have the majority of power. As a final point, it is clear that the SGWB is best constrained around a frequency of 4 mHz, where the power of the GB is less and the uncertainty in the instrumental noise is also the largest (although still small) at this point. This can be understood from Fig. 6, which shows that the power law background is closest to the instrumental noise ASD at that frequency and the Galactic binaries pick at 1 mHz, and so this frequency range dominates the SNR in the signal. We expect to be able to measure the background best in the frequency range where it is most dominant relative to the instrumental noise and distinguishable from the Galactic binaries.

#### IV. DISCUSSION AND CONCLUSION

We have explored the impact of noise knowledge uncertainty on measuring the parameters of various modeled stochastic gravitational wave backgrounds. This was done by modeling instrumental noise uncertainties using cubic splines to represent deviations away from the design PSDs and CSDs for the three TDI channels *A*, *E*, and  $\zeta$ . We then used a Fisher matrix analysis to evaluate the expected uncertainties in the measurements of the model parameters when fitting a model including the instrumental noise uncertainties and compared it to fitting a model without those uncertainties. The degree of uncertainty was characterized by including a Gaussian prior on the instrumental noise parameters, allowing us to quantify the impact of imposing a requirement on our noise knowledge.

This analysis showed that, for all SGWB models, allowing for instrumental noise uncertainties leads to a significant increase in the uncertainty in our measurements of the background parameters. The increase in uncertainty was a factor of 2–8 for the Gaussian bump model, which reduces to 2–4 when not including GB as foreground, 55–60 for the power law (15–30 without GB as foreground), 20–35 for the first-order phase transition (20–50 without GB as foreground), and 30–75 for the power law with running

(20–75 without GB as foreground). These increased uncertainties correspond to the threshold background energy density required for detection increasing by a factor of 10 (5 without GB) for the Gaussian bump model, a factor of 60 with and without GB for the power with running, and a factor of 20 with and without GB for all other models (50 for the power law when including GBs). The threshold energy density at 1 mHz at which the backgrounds start to be detectable are  $4 \times 10^{-13}$ ,  $4 \times 10^{-13}$ ,  $2 \times 10^{-16}$ , and  $10^{-12}$  ( $10^{-13}$ ,  $2.5 \times 10^{-13}$ ,  $8 \times 10^{-17}$ , and  $5 \times 10^{-13}$  if we do not include the GB foreground) for the power law, power law with running, Gaussian bump, and FOPT models, respectively. Comparing these to the reference background amplitudes introduced in Sec. II F, we see that the power law, the Gaussian bump, and FOPT backgrounds are detectable at the reference amplitudes, while the power law with running is not, as the threshold energy density is 1.5 times higher than the reference. However, for this latter background, the amplitudes were specified based on the SNR and not on a physical model. The reference amplitudes for the power law and FOPT backgrounds are based on physical model predictions, so it is more important that these backgrounds are still detectable. We note that this result does depend on the particular choice of the model we used for representing the instrumental noise uncertainty. If this model is made even more flexible, for example, by increasing the number of spline knots used, the threshold would increase further and potentially also make the reference backgrounds undetectable.

When we vary our assumed level of knowledge of the instrumental noise, we find that the uncertainties on the SGWB parameters show a similar trend for all models, starting to degrade at relatively small uncertainties, increasing, and then saturating after a certain point. The point at which the sensitivity starts to degrade is when the uncertainty in the log-spectral density of the noise reaches  $\sim 10^{-6} - 10^{-5}$ , depending on the SGWB model. The uncertainty saturates at log-spectral density uncertainties of  $\sim 10^{-2}$ ,  $10^{-1}$ ,  $10^{-2}$ , and  $10^1$  ( $10^{-2}$ ,  $10^{-1}$ ,  $10^{-3}$ , and  $10^{-1}$  in the absence of the GB foreground) for the power law, power law with running, Gaussian bump, and FOPT backgrounds, respectively. This means that if we wanted to limit the degradation in the science that arises from lack of noise knowledge, we would have to impose a very stringent requirement on our knowledge of the noise. This is likely to be impossible to implement in practice, so we will have to accept that our ability to resolve SGWBs will not be as good as calculations that assume perfect noise knowledge prediction.

It is important to note that these results are based on some assumptions which might not hold in practice. In particular, we have considered only modeled SGWBs, and we have assumed a particular form for variations in the PSD that forces variations to be smoothly varying as a function of frequency. We have also run additional tests for

completeness, which are not reported in the paper for reasons of conciseness, where we have increased the number of knots. Increasing the number of knots provides a more flexible instrumental noise model, allowing potentially faster variations of the PSD as a function of frequency. This leads to a degradation in the estimation of the log-energy density of the SGWB components. It is the distinguishability of the models that allows us to measure the parameters of the SGWBs. In the extreme picture where we do not want to make any assumption at all about the form of the instrumental or SGWB spectral densities, then spectral separation will not be possible. We will be able to report measured power spectral density in all channels, and cross-spectral densities between them, and translate these into upper limits on the SGWB amplitude, but any interpretation of this as an actual detection will require independent confirmation from another detector [16].

All previous studies of the separation of instrumental noise and stochastic backgrounds have required assumptions: In [25], it was assumed that the instrumental uncertainty is a spline and that the SGWB has a power law spectrum; in [11], it was assumed that the instrumental noise is determined by 12 individual noise levels; and in this paper, we are assuming something similar to [25], although with a bit more flexibility, a wider variety of SGWB models and a different noise model for single satellite links. The SGWBinner [7] is agnostic on the spectrum of the background, but it can work only because it assumes a specific model for the instrumental noise. That is not going to be possible in practice. SGWBinner could be adapted to use a more flexible noise model, similar to the model used here, but the precision of the background recovery will be degraded. If we have a completely general instrumental noise model and a completely general SGWB model, then we will not be able to separate them. In that case, the only hope would be that the SGWB is above the design sensitivity, and we trust that the instrumental noise meets the mission requirements, in which case the best interpretation of such an observation would be an SGWB. However, even then an assumption would be made that the mission had met the design sensitivity requirements.

An exploration of how our ability to separate instrumental noise from SGWB, as the spectral models of the SGWB and the instrumental noise are made more complicated, should be the focus of future work. Moreover, there are a couple of issues that we have not explored in this paper which should also be the subject of future studies. First, we have ignored the possible presence of correlations across frequencies in the stochastic background spectra. Such correlations could arise from nonstationarities or nonstandard physics. In general, we would expect that well-modeled correlations could help to break degeneracies and, hence, improve the precision of parameter estimation. An example of a well-modeled nonstationarity would be the time dependence of the Galactic binary background. Accounting for unmodeled stationarities

would introduce additional model parameters, fitting for which would tend to reduce the precision of parameter estimation of the original parameters, so this would probably make the sensitivity somewhat worse. In this paper, we did consider one type of correlation, which was the correlation between the instrumental noise in different TDI channels. The inclusion of this had little impact on the precision of parameter estimation, because we limited the size of the correlation to 10% of the uncorrelated noise level. This limit was well motivated, but if much larger correlations were present, in either the instrumental noise or astrophysical background, we would expect to see degradation in parameter estimation precision. Another simplification that was made in the analysis presented in this paper was that we considered only one type of stochastic background at a time, while the LISA data could contain backgrounds with several different origins. A realistic scenario would be that the data include backgrounds from Galactic binaries, stellar-origin black holes, and one or more cosmological stochastic backgrounds. A full analysis of LISA data would have to include the possibility of fitting multiple backgrounds at the same time, ideally in a flexible way that allows the number and properties of the backgrounds to be automatically adapted to the observed data. In general, we would expect fitting multiple backgrounds to lead to the precision of parameter estimation for each background to degrade. However, the amount of degradation will depend on the degree of similarity of the shapes of the different backgrounds. We saw the effect of this when removing the Galactic binary foreground (see Appendix C for details). Figure 12 shows that the biggest effect of removing the foreground is for the Gaussian bump and power law backgrounds. These are the backgrounds that look most similar to the Galactic background in the frequency range where most of the SNR is accumulated. We would expect this to be generally true—if we are fitting multiple backgrounds that have similar spectral shapes, there will be bigger degeneracies than when fitting more distinct backgrounds. Further studies would be required to obtain a quantitative assessment of the amount of degradation arising from this and the correlations discussed in the previous paragraph.

*Note added.* In [57], it is used a known spectral shape for the noise, with a frequency-independent uncertainty on its amplitude in the range 1% to 20%, and they remain fully agnostic on the signal. The authors also compute lower bounds on the signal amplitude as a function of the uncertainty on the noise amplitude in a set of frequency bins such that it be detectable with a Bayes factor greater than 100.

## ACKNOWLEDGMENTS

M. M. gratefully acknowledges the support of the German Space Agency, DLR. The work is supported by the Federal Ministry for Economic Affairs and Climate Action based on

a resolution of the German Bundestag (Project Ref. No. FKZ 50 OQ 2301). The authors thank Chiara Caprini for her review and suggestions regarding the use of SGWB templates in the text. Additionally, we acknowledge Mauro Pieroni for providing feedback on the presented results and the implementation of spline models. Furthermore, we thank Olaf Hartwig for discussions on the accurate computation of the GW transfer function and the noise models and Marc Lilley for comparisons on the results obtained with the Fisher matrix formalism. We thank Lorenzo Sala for feedback on the recent analysis of the LISA-Pathfinder performance results. The scientific discussions with Quentin Baghi, Jean Baptiste Bailey, Germano Nardini, Nikolaos Karnesis, Jesus Torrado, Nam Dam Quam, Henry Hinshauspe, Antoine Petiteau, and Riccardo Buscicchio have also been highly appreciated. Their feedback on the results and methodology presented in the paper has been valuable for the outcome. We also thank the two anonymous referees for improving the quality of the manuscript.

## APPENDIX A: LIKELIHOOD DERIVATION

We derive the likelihood starting from the noise properties and explain why it takes the form shown in Sec. II. If we assume that the real-time series  $n(t)$  is a stationary, zero-mean, Gaussian, and ergodic random process, then the Fourier transform of the noise  $\tilde{n}_k = \tilde{n}(f_k)$  at each frequency  $f_k$  is normally distributed with zero mean and variance  $\sigma_k^2$ . Thus, the natural log-likelihood at each frequency takes the form of a two-dimensional normal distribution

$$\ln p(\tilde{n}_k) = -\frac{1}{2} \left( \frac{\text{Re}[\tilde{n}_k]^2}{\sigma_k^2} + \frac{\text{Im}[\tilde{n}_k]^2}{\sigma_k^2} \right) - \frac{1}{2} \ln[(2\pi\sigma_k^2)^2], \quad (\text{A1})$$

where we assumed that the real Re and imaginary Im parts of the noise are not correlated and have the same variance. If we further assume that the variance of the noise at different frequencies follows a one-sided power spectral density  $S_n(f)$ , then

$$\langle \tilde{n}^*(f') \tilde{n}(f) \rangle = \frac{1}{2} S_n(f) \delta(f - f'), \quad (\text{A2})$$

$$\langle \tilde{n}(f') \tilde{n}(f) \rangle = 0, \quad (\text{A3})$$

where we used the expectation value of  $\langle \rangle$  over the data-generating process. For a set of frequencies, the first relation can be written as

$$\langle \tilde{n}_k^* \tilde{n}_j \rangle = \frac{T}{2} S_n(f_k) \delta_{jk}. \quad (\text{A4})$$

Therefore, the variance of the real and imaginary parts of the noise is given by

$$\langle \text{Re}[\tilde{n}_k]^2 \rangle = \langle \text{Im}[\tilde{n}_k]^2 \rangle = \frac{T}{4} S_n(f_k) = \sigma_k^2. \quad (\text{A5})$$

We can write the natural log-likelihood for all the measured frequencies as

$$\sum_k \ln p(\tilde{n}_k) = -\sum_{k=1}^n \ln \left[ 2\pi \frac{T}{4} S_n(f_k) \right] - \frac{1}{2} \sum_{k=1}^n \frac{|\tilde{n}(f_k)|^2}{S_n(f_k)}, \quad (\text{A6})$$

which becomes in the continuum limit

$$\ln p(\tilde{n}) = -\ln \left[ 2\pi \frac{1}{4} \det[S_n(f) \delta(f - f')] \right] - \frac{1}{2} \int_0^\infty \frac{|\tilde{n}(f)|^2}{S_n(f)} df. \quad (\text{A7})$$

Note that in the continuum limit the variance of the noise can be thought of as an operator. One can define the inner product

$$(a(t)|b(t)) = 4\text{Re} \int_0^\infty \int_0^\infty \tilde{a}^*(f) \Sigma^{-1}(f, f') \tilde{b}(f') df df' \quad (\text{A8})$$

with  $\Sigma^{-1}$  defined through the relation

$$\int_0^\infty \Sigma^{-1}(f, f') \Sigma(f', f'') df' = \delta(f - f''), \quad (\text{A9})$$

where, if we set in Eq. (A9) that  $\Sigma(f', f'') = \delta(f' - f'') S_n(f')$ , we obtain

$$\Sigma^{-1}(f, f'') S_n(f'') = \delta(f - f'') \quad (\text{A10})$$

and the inner product becomes

$$(a(t)|b(t)) = 4\text{Re} \int_0^\infty \int_0^\infty \frac{\tilde{a}^*(f) \delta(f - f') \tilde{b}(f')}{S_n(f')} df df' = 4\text{Re} \int_0^\infty \frac{\tilde{a}^*(f) \tilde{b}(f)}{S_n(f)} df. \quad (\text{A11})$$

## APPENDIX B: FISHER MATRIX DERIVATION

### 1. Single detector

To compute the Fisher matrix of Eq. (7), we need the first derivative of the log-likelihood  $l$  with respect to the parameters of the power spectral density.

Here, we present the derivation of the Fisher matrix for the noise parameters  $\vec{\lambda}$  affecting the one-sided spectral density  $S_n(f|\vec{\lambda})$ , but this can be easily extended also including the gravitational wave background parameters  $S_n(f|\vec{\lambda}) \rightarrow S_n(f|\vec{\lambda}) + S_{\text{GW}}(f|\vec{\theta})$ . We differentiate the log-likelihood of Eq. (A6) with respect to the parameters  $\vec{\lambda}$ :

$$\frac{\partial l}{\partial \lambda^i} = \sum_{k=1}^n \left[ -\frac{1}{S_n(f_k)} \frac{\partial S_n(f_k)}{\partial \lambda^i} + \frac{1}{2} \frac{|\tilde{n}(f_k)|^2}{S_n(f_k)^2} \frac{\partial S_n(f_k)}{\partial \lambda^i} \right], \quad (\text{B1})$$

where we have omitted the dependency on  $\vec{\lambda}$  to have a lighter notation. The second derivative of the likelihood is then

$$\begin{aligned} \frac{\partial^2 l}{\partial \lambda^i \partial \lambda^j} = & \sum_{k=1}^n \left[ \frac{1}{S_n^2(f_k)} \frac{\partial S_n(f_k)}{\partial \lambda^i} \frac{\partial S_n(f_k)}{\partial \lambda^j} - \frac{1}{S_n(f_k)} \frac{\partial^2 S_n(f_k)}{\partial \lambda^i \partial \lambda^j} \right. \\ & - \frac{1}{2} \frac{2|\tilde{n}(f_k)|^2}{S_n(f_k)^3} \frac{\partial S_n(f_k)}{\partial \lambda^j} \frac{\partial S_n(f_k)}{\partial \lambda^i} \\ & \left. + \frac{1}{2} \frac{|\tilde{n}(f_k)|^2}{S_n(f_k)^2} \frac{\partial^2 S_n(f_k)}{\partial \lambda^j \partial \lambda^i} \right]; \end{aligned} \quad (\text{B2})$$

using the definition of Eq. (A4) the second and last terms cancel, and we get

$$\Gamma_{ij} = \sum_{k=1}^n \frac{1}{S_n(f_k)^2} \frac{\partial S_n(f_k)}{\partial \lambda^i} \frac{\partial S_n(f_k)}{\partial \lambda^j}. \quad (\text{B3})$$

If we want to get the continuum limit, we need to recast a factor of  $T$  df:

$$\Gamma_{ij} = T \int_0^\infty \frac{1}{S_n(f)^2} \frac{\partial S_n(f)}{\partial \lambda^i} \frac{\partial S_n(f)}{\partial \lambda^j} df. \quad (\text{B4})$$

## 2. Multiple detectors: Real and imaginary part as separate random variables

If we want to generalize our derivation to multiple detectors or channels, we need to define the noise properties of each channel. For simplicity, let us consider two channels  $A$  and  $E$  with four independent random variables  $X(f_k) = X_k = \{\text{Re}[\tilde{X}_k^A], \text{Im}[\tilde{X}_k^A], \text{Re}[\tilde{X}_k^E], \text{Im}[\tilde{X}_k^E]\}$  at each frequency  $f_k$ . Since the final likelihood will be given by the product over all the frequencies, we consider only one frequency and we drop the subscript “ $k$ .” We can specify the spectral densities of each channel and the cross-spectral densities with

$$\langle \tilde{X}^{c*}(f') \tilde{X}^c(f) \rangle = \frac{1}{2} S_c(f) \delta(f - f'), \quad (\text{B5a})$$

$$\langle \tilde{X}^c(f') \tilde{X}^c(f) \rangle = 0, \quad (\text{B5b})$$

$$\langle \tilde{X}^{E*}(f') \tilde{X}^A(f) \rangle = \frac{1}{2} S_{AE}^*(f) \delta(f - f'), \quad (\text{B5c})$$

$$\langle \tilde{X}^{A*}(f') \tilde{X}^E(f) \rangle = \frac{1}{2} S_{AE}(f) \delta(f - f'), \quad (\text{B5d})$$

$$\langle \tilde{X}^A(f') \tilde{X}^E(f) \rangle = 0, \quad (\text{B5e})$$

where the first two rows are valid for both channels  $c = A, E$  and  $S_c$  is real and  $S_{AE}$  is complex. From the above expression, we can deduce for the discrete case

$$\langle \text{Re}[\tilde{X}_c] \text{Re}[\tilde{X}_c] \rangle + \langle \text{Im}[\tilde{X}_c] \text{Im}[\tilde{X}_c] \rangle = T \frac{S_c}{2}, \quad (\text{B6a})$$

$$\langle \text{Re}[\tilde{X}_c] \text{Re}[\tilde{X}_c] - \text{Im}[\tilde{X}_c] \text{Im}[\tilde{X}_c] \rangle = 0, \quad (\text{B6b})$$

$$\langle \text{Re}[\tilde{X}_c] \text{Im}[\tilde{X}_c] \rangle = 0, \quad (\text{B6c})$$

$$\langle \text{Re}[\tilde{X}_A] \text{Re}[\tilde{X}_E] \rangle + \langle \text{Im}[\tilde{X}_A] \text{Im}[\tilde{X}_E] \rangle = T \frac{\text{Re}[S_{AE}]}{2}, \quad (\text{B6d})$$

$$\langle \text{Re}[\tilde{X}_A] \text{Re}[\tilde{X}_E] - \text{Im}[\tilde{X}_A] \text{Im}[\tilde{X}_E] \rangle = 0, \quad (\text{B6e})$$

$$\langle \text{Re}[\tilde{X}_A] \text{Im}[\tilde{X}_E] \rangle - \langle \text{Im}[\tilde{X}_A] \text{Re}[\tilde{X}_E] \rangle = T \frac{\text{Im}[S_{AE}]}{2}, \quad (\text{B6f})$$

$$\langle \text{Re}[\tilde{X}_A] \text{Im}[\tilde{X}_E] \rangle + \langle \text{Im}[\tilde{X}_A] \text{Re}[\tilde{X}_E] \rangle = 0, \quad (\text{B6g})$$

where  $T$  is the observation time and in the first three rows  $c = A, E$ . Note that these are in total ten independent conditions (three equations for  $A$ , three equations for  $E$ , and four equations for  $AE$ ) that specify uniquely the ten independent elements of a symmetric covariance matrix.

For a single frequency, we can generalize the likelihood to two channels:

$$p(X) = \frac{1}{\sqrt{(2\pi)^{2 \times N_c} \det(T\Sigma)}} e^{-\frac{1}{2T} X^\top \Sigma^{-1} X}, \quad (\text{B7})$$

where  $N_c = 2$  is the number of channels,  $X$  is a four-dimensional vector defined above, and  $\Sigma$  is the multiple-channels covariance matrix:

$$\Sigma = \begin{pmatrix} \frac{S_A}{4} & 0 & \frac{\text{Re}(S_{AE})}{4} & \frac{\text{Im}(S_{AE})}{4} \\ 0 & \frac{S_A}{4} & \frac{\text{Im}(S_{AE})}{4} & \frac{\text{Re}(S_{AE})}{4} \\ \frac{\text{Re}(S_{AE})}{4} & \frac{\text{Im}(S_{AE})}{4} & \frac{S_E}{4} & 0 \\ \frac{\text{Im}(S_{AE})}{4} & \frac{\text{Re}(S_{AE})}{4} & 0 & \frac{S_E}{4} \end{pmatrix}, \quad (\text{B8})$$

where each element is evaluated at a fixed frequency. It can be shown that the expectation value of the argument of the exponential  $X^\top \Sigma^{-1} X / T$  equals the degrees of freedom, in this case, 4. We have two channels, where each one has two degrees of freedom associated with the real and imaginary part of  $\tilde{X}$ .

We can then derive the Fisher matrix for the multiple-channel case. Taking the first derivative of the log-likelihood

$$\frac{\partial \ln p(X)}{\partial \lambda^i} = -\frac{1}{2} \frac{1}{\det(\Sigma)} \frac{\partial \det(\Sigma)}{\partial \lambda^i} - \frac{1}{2T} X^\top \frac{\partial \Sigma^{-1}}{\partial \lambda^i} X, \quad (\text{B9})$$

where we can use the following property of the determinant:

$$\begin{aligned} \frac{\partial \det(\Sigma)}{\partial \lambda^i} &= \det(\Sigma) \text{Tr} \left[ \Sigma^{-1} \frac{\partial \Sigma}{\partial \lambda^i} \right] \\ &= \det(\Sigma) [\Sigma^{-1}]_{lm} \left[ \frac{\partial \Sigma}{\partial \lambda^i} \right]^{ml} \end{aligned} \quad (\text{B10})$$

to obtain

$$\frac{\partial \ln p(X)}{\partial \lambda^i} = -\frac{1}{2} [\Sigma^{-1}]_{lm} \left[ \frac{\partial \Sigma}{\partial \lambda^i} \right]^{ml} - \frac{1}{2T} X^T \frac{\partial \Sigma^{-1}}{\partial \lambda^i} X. \quad (\text{B11})$$

Then, the second derivative of the log-likelihood takes the form

$$\begin{aligned} \frac{\partial^2 \ln p(X)}{\partial \lambda^i \partial \lambda^j} &= -\frac{1}{2} \frac{\partial (\Sigma^{-1})^{lm}}{\partial \lambda^i} \frac{\partial \Sigma_{ml}}{\partial \lambda^j} \\ &\quad - \frac{1}{2} \Sigma_{lm}^{-1} \frac{\partial^2 \Sigma^{ml}}{\partial \lambda^i \partial \lambda^j} - \frac{1}{2T} X^T \frac{\partial^2 \Sigma^{-1}}{\partial \lambda^i \partial \lambda^j} X. \end{aligned} \quad (\text{B12})$$

We can take the expectation value of the previous expression and obtain the Fisher matrix for a single frequency with

$$\Gamma_{ij} = \frac{1}{2} \left[ \frac{\partial \Sigma_{lm}^{-1}}{\partial \lambda^i} \frac{\partial \Sigma^{ml}}{\partial \lambda^j} + \Sigma_{lm}^{-1} \frac{\partial^2 \Sigma^{ml}}{\partial \lambda^i \partial \lambda^j} + \Sigma_{ml} \frac{\partial^2 (\Sigma^{-1})^{lm}}{\partial \lambda^i \partial \lambda^j} \right], \quad (\text{B13})$$

where we have considered  $\langle X_l^T \frac{\partial^2 \Sigma_{lm}^{-1}}{\partial \lambda^i \partial \lambda^j} X_m \rangle \frac{1}{T} = \frac{\partial^2 \Sigma_{lm}^{-1}}{\partial \lambda^i \partial \lambda^j} \Sigma_{ml}$ . If we use the property

$$\frac{\partial (\Sigma^{-1})_{lm}^{-1}}{\partial \lambda} = -(\Sigma^{-1})_{ln}^{-1} \frac{\partial (\Sigma)_{nq}}{\partial \lambda} (\Sigma^{-1})_{qm}^{-1}, \quad (\text{B14})$$

we obtain the following expression:

$$\Gamma_{ij} = \frac{1}{2} \text{Tr} \left[ -\Sigma^{-1} \frac{\partial \Sigma}{\partial \lambda^i} \Sigma^{-1} \frac{\partial \Sigma}{\partial \lambda^j} + \Sigma^{-1} \frac{\partial^2 \Sigma}{\partial \lambda^i \partial \lambda^j} + \Sigma \frac{\partial^2 \Sigma^{-1}}{\partial \lambda^i \partial \lambda^j} \right], \quad (\text{B15})$$

which can be further simplified if we use the following properties:

$$\partial(\Sigma \Sigma^{-1}) = 0, \quad (\text{B16a})$$

$$\partial \Sigma \Sigma^{-1} + \Sigma \partial \Sigma^{-1} = 0, \quad (\text{B16b})$$

$$\partial^2 \Sigma \Sigma^{-1} + 2\partial \Sigma \partial \Sigma^{-1} + \Sigma \partial^2 \Sigma^{-1} = 0, \quad (\text{B16c})$$

$$\partial^2 \Sigma \Sigma^{-1} - 2\partial \Sigma \Sigma^{-1} \partial \Sigma \Sigma^{-1} + \Sigma \partial^2 \Sigma^{-1} = 0. \quad (\text{B16d})$$

Note that, in the above expression, the first and last terms of Eq. (B16d) correspond to the last two terms in the Fisher matrix expression (B15). The final expression for all

frequencies can be easily obtained by taking the sum over all the frequencies:

$$\Gamma_{ij} = \frac{1}{2} \sum_{k=1}^n \left[ (\Sigma_k^{-1})_{lr} \frac{\partial \Sigma_k^{rp}}{\partial \lambda^i} (\Sigma_k^{-1})_{pm} \frac{\partial \Sigma_k^{ml}}{\partial \lambda^j} \right]. \quad (\text{B17})$$

Note that there is an additional factor of 1/2 with respect to Eq. (B3). If we insert only the first two columns and rows of  $\Sigma$ , we obtain the previous equation for the single channel as expected.

### 3. Multiple detectors: Complex random variables

Equivalently, the likelihood can be written in terms of complex variables  $\tilde{X}_A$  and  $\tilde{X}_E$  [58]:

$$p(\tilde{X}_A, \tilde{X}_E) = \frac{e^{-\frac{1}{2}([\tilde{X}_A, \tilde{X}_E]^H \Sigma^{-1} [\tilde{X}_A, \tilde{X}_E])}}{(2\pi)^{N_c} \det(T\Sigma)}, \quad (\text{B18})$$

where ‘‘H’’ indicates the Hermitian conjugate, the factor of 1/2 disappeared because it is a complex distribution and must match Eqs. (B7) and (B8), and the new complex covariance matrix is defined as

$$\Sigma = \frac{1}{2} \begin{pmatrix} S_A & S_{AE} \\ S_{AE}^* & S_E \end{pmatrix}, \quad (\text{B19})$$

where  $\Sigma$  is now a Hermitian matrix and can be obtained from the conditions imposed in Eqs. (B5). The expectation value of  $([\tilde{X}_A, \tilde{X}_E]^H \Sigma^{-1} [\tilde{X}_A, \tilde{X}_E])/T$  over complex variable realizations  $[\tilde{X}_A, \tilde{X}_E]$  is now 2. However, since the exponential does not have any factor of 1/2 for a complex distribution, we recover the same number of degrees of freedom in the argument of the exponent as in the previous derivation; i.e., we got  $\exp[\frac{1}{2}4]$  for the case of multiple detectors with real and imaginary parts as separate random variables and  $\exp[2]$  for the case considered here.

The derivation of the Fisher matrix differs from the previous one [Eq. (B17)] only by the factor 1/2:

$$\Gamma_{ij} = \sum_{k=1}^n \left[ (\Sigma_k^{-1})_{lr} \frac{\partial \Sigma_k^{rp}}{\partial \lambda^i} (\Sigma_k^{-1})_{pm} \frac{\partial \Sigma_k^{ml}}{\partial \lambda^j} \right], \quad (\text{B20})$$

where the matrix  $\Sigma_k$  is given by  $\Sigma$  with spectral densities evaluated at given frequency  $f_k$ .

Note that we can recover the single channel realization by using the first element of  $\Sigma$ .

The continuum limit of the Fisher matrix in this formulation is given by

$$\Gamma_{ij} = T \int_0^\infty (\Sigma_k^{-1})_{lr} \frac{\partial \Sigma_k^{rp}}{\partial \lambda^i} (\Sigma_k^{-1})_{pm} \frac{\partial \Sigma_k^{ml}}{\partial \lambda^j} df. \quad (\text{B21})$$

#### 4. Deterministic sources and noise cross-correlation

In the presence of a deterministic source  $\tilde{h}(f_k|\vec{\mu})$ , the derivative of the log-likelihood in Eq. (6) with respect to the source parameters  $\vec{\mu}$  is

$$\frac{\partial l}{\partial \mu^i} = - \sum_{k=1}^n \frac{|\tilde{s}(f_k) - \tilde{h}(f_k|\vec{\mu})|}{\frac{\pi}{4} S_n(f_k|\vec{\lambda})} \frac{\partial \tilde{h}(f_k|\vec{\mu})}{\partial \mu^i}, \quad (\text{B22})$$

and the derivative with respect to the parameters characterizing the spectral density is given by Eq. (B1). The derivative with respect to the source parameters is odd in the noise component,  $\tilde{n}(f_k) = \tilde{s}(f_k) - \tilde{h}(f_k|\vec{\mu})$ , while the derivative with respect to the noise parameters is even. Since  $\mathbb{E}[\tilde{n}(f_k)] = 0$ , from this we deduce that

$$\mathbb{E}_{\mathcal{L}} \left[ \frac{\partial l}{\partial \mu^i} \frac{\partial l}{\partial \lambda^j} \right] = 0; \quad (\text{B23})$$

i.e., at this level of approximation, the terms in the Fisher matrix that mix signal and noise parameters vanish. We conclude that the estimation of the noise parameters and the signal parameters is, in leading order, independent. Lack of knowledge of the noise should, therefore, not significantly affect measurements of the parameters of deterministic sources, except indirectly through the change in the spectral density that enters the likelihood for the deterministic sources.

### APPENDIX C: IMPACT OF INSTRUMENTAL NOISE KNOWLEDGE UNCERTAINTY ON SGWB RECOVERY IN ABSENCE OF GALACTIC FOREGROUND

Below, we show the same computations we did in Sec. III but in case we do not consider the presence of the foreground.

#### 1. Power law

Figure 18 shows the results computed for the power law model. We see that, in the presence of instrumental noise uncertainties, the uncertainty in the SGWB parameters increases by a factor of  $\sim 19$ – $36$ , with the uncertainty in the slope being more affected than that of the amplitude. Considering the raw uncertainties, to achieve the same measurement precision, the background energy density would have to be  $\sim 33$  times larger than it would need to be in the absence of noise knowledge uncertainties. However, a background with an amplitude equal to the reference value should be detectable even allowing for confusion with instrumental noise mismodeling.

#### 2. Power law with running

The results for this model are shown in Fig. 19. In this case, we see that the uncertainties in the SGWB parameters

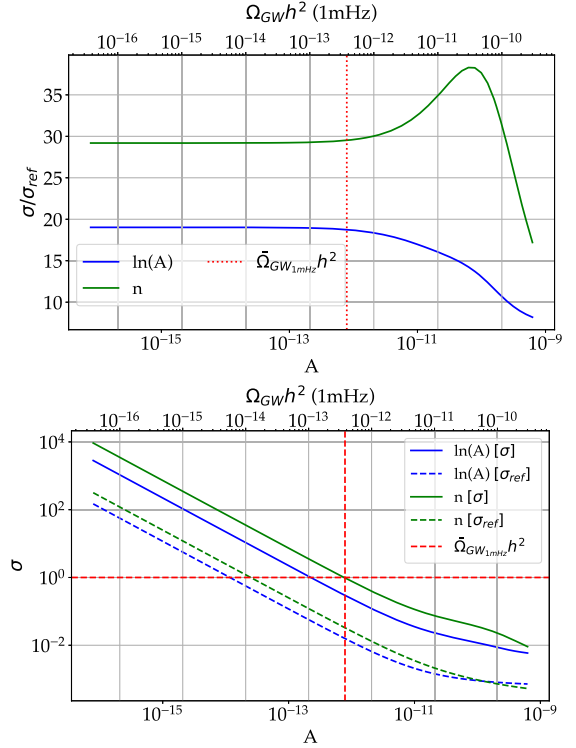


FIG. 18. Results for the power law SGWB model without foreground.

increase by a factor of  $\sim 21$ – $72$ , with the uncertainty on the log amplitude being most affected in this case. Once again, the relative increase in the uncertainty is somewhat lower at higher background amplitudes. The lower panel in Fig. 19 shows that the background is not detectable at the reference amplitude. An energy density  $\sim 5$  times higher would be required for detection. In general, the background again has to have an energy density  $\sim 100$  times higher to be characterized with the same measurement precision when there is instrumental noise uncertainty as it could be without those uncertainties.

#### 3. Gaussian bump

The results for this model are shown in Fig. 20. In this case, the degradation in the precision of parameter measurement is a factor of  $\sim 2.3$ – $4$  when allowing for lack of knowledge of the instrumental noise. From the lower panel in Fig. 20, we see that the energy density in a Gaussian bump SGWB has to be just a small factor of  $\sim 2.5$  times bigger to achieve the same measurement precision when the instrumental noise is not known perfectly. Moreover, a Gaussian bump background at the reference amplitude can be measured to percent precision at the reference amplitude. The width of the Gaussian can be measured to a few tens of percent precision at the reference amplitude, improving approximately linearly with the background energy density.

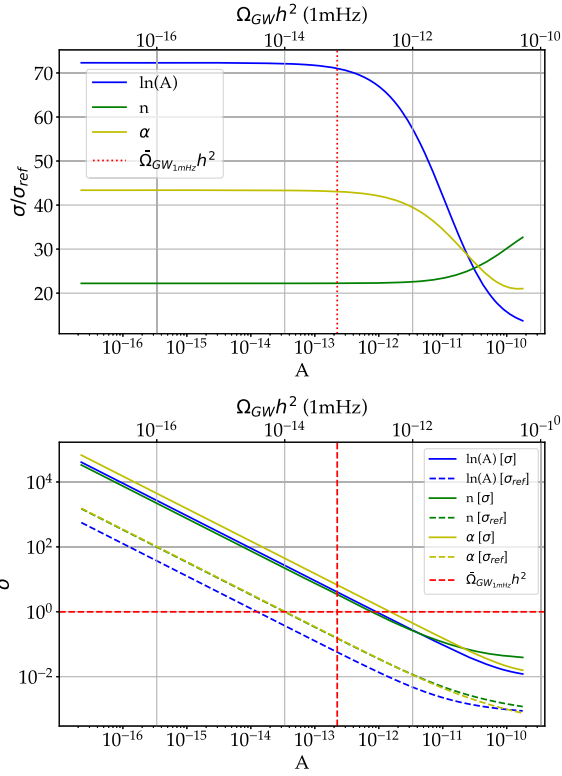


FIG. 19. Results for the power law with running SGWB model without foreground.

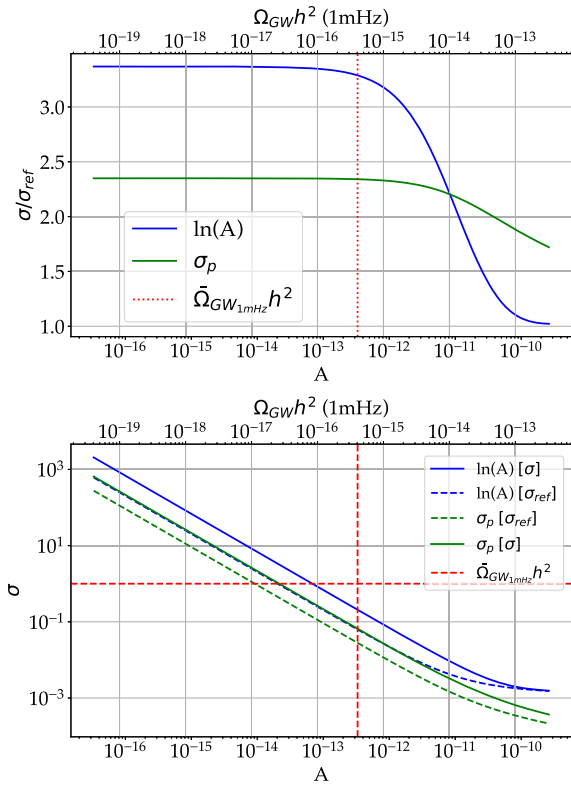


FIG. 20. Results for Gaussian bump SGWB model without foreground.

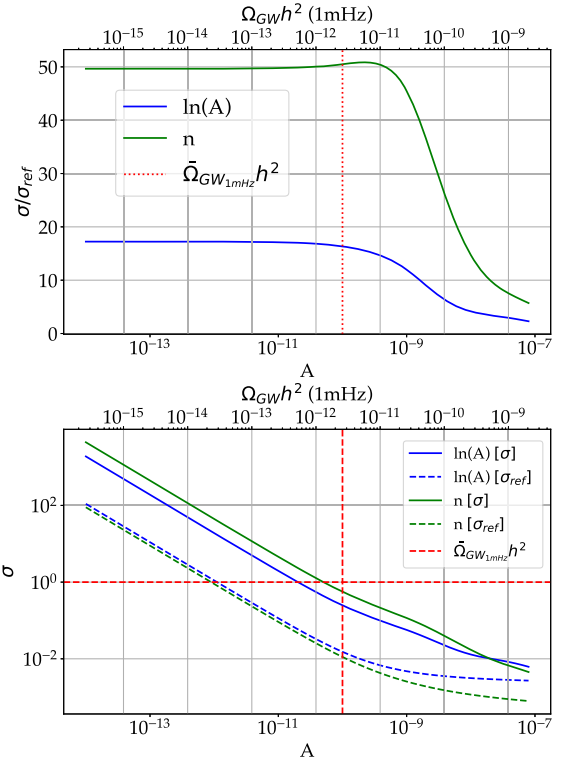


FIG. 21. Results for first-order phase transition SGWB model without foreground.

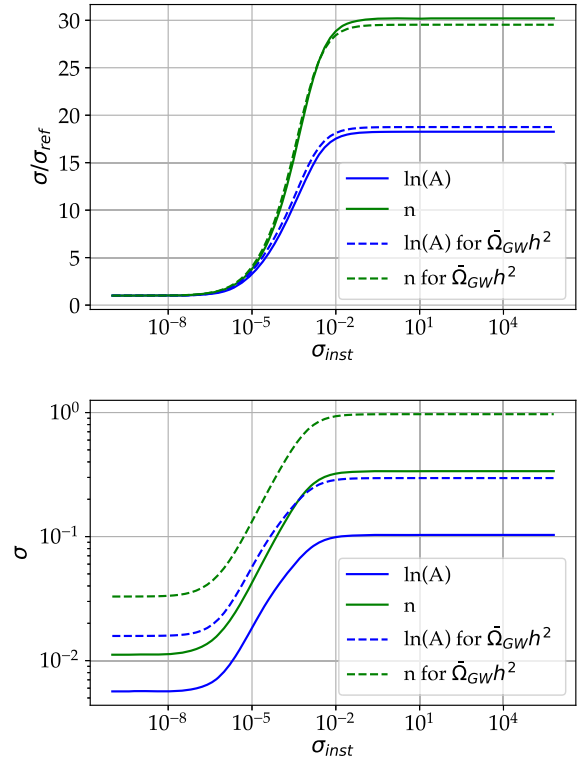


FIG. 22. As in Fig. 18 but now for fixed background amplitude and varying the variance of the Gaussian prior on the instrumental noise spline model. This plot is for a power law background, and the amplitude has been fixed such that the SNR in TDI channel A is 136 (continuous lines) and 43 (dashed lines).

### 4. First-order phase transition

The results for first-order phase transition are shown in Fig. 21. The results for this SGWB model are quite similar to those for the power law background. When allowing for instrumental noise knowledge uncertainties, the precision with which the SGWB log amplitude can be characterized degrades by a factor of  $\sim 18$ . The degradation in the determination of the spectral index is even larger,  $\sim 50$ . Once again, to achieve the same measurement precision, the background energy density would have to be  $\sim 50$  times larger than it would need to be in the absence of noise knowledge uncertainties. Nonetheless, a FOPT background at the reference amplitude would still be detectable and provide a measurement of the spectral index at the level of about 0.5%.

We can do the same analysis we did in Sec. III B but without including the foreground. The results for all four SGWB models are qualitatively similar among themselves and also to the previous case with foreground in Sec. III B. Figure 22 considers the power law case, Fig. 23 the case of power law with running, Fig. 24 the case of Gaussian model, and Fig. 25 the case of FOPT model.

The main conclusion from these results is that again if we wanted to ensure that there was no degradation in LISA science due to lack of noise knowledge, the requirement on the noise knowledge would be  $\ll 10\%$ .

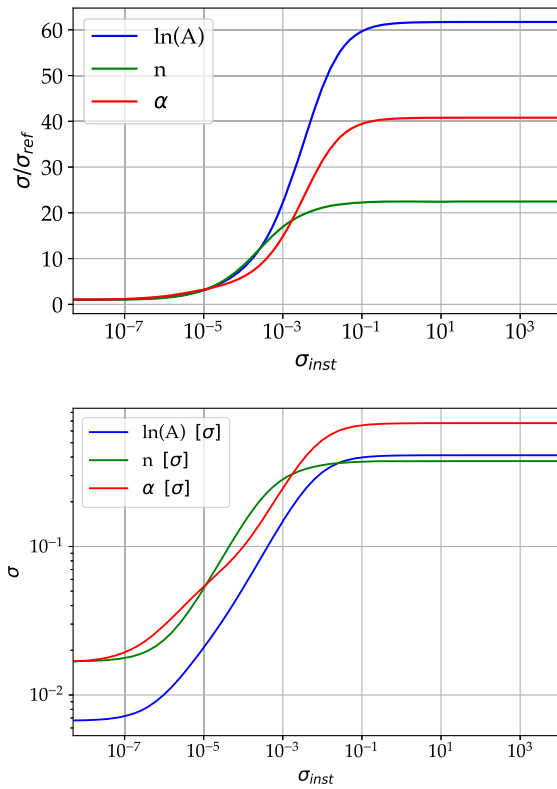


FIG. 23. As in Fig. 22 but now for the power law with running model. The background amplitude has been fixed to give an overall SNR of 145.

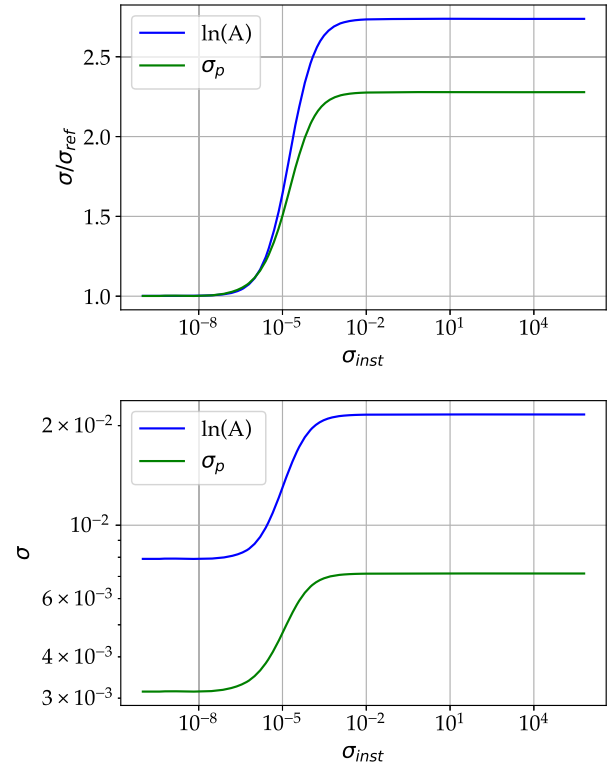


FIG. 24. As in Fig. 22 but now for the Gaussian bump model. The background amplitude has been fixed to give an overall SNR of 135.

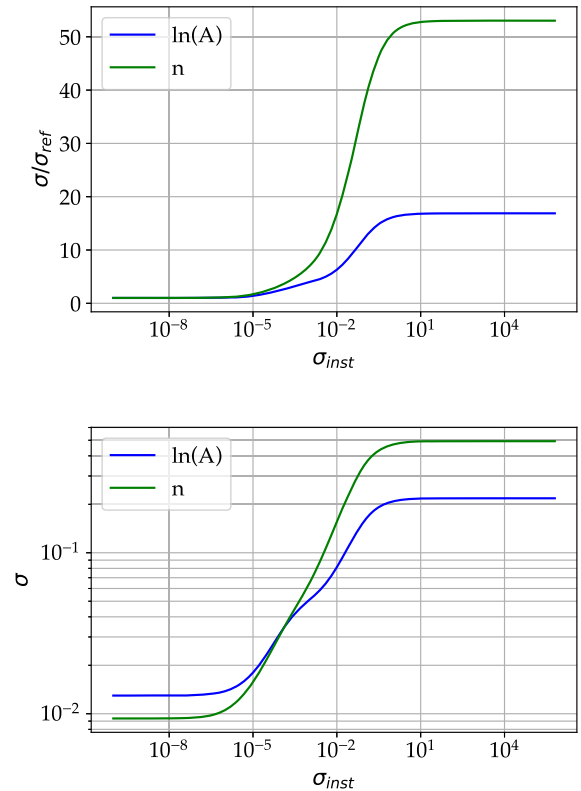


FIG. 25. As in Fig. 22 but now for the FOPT model. The background amplitude has been fixed to give an overall SNR of 149.

### 5. Signal reconstruction without foreground of Galactic binaries

We consider a power law signal with an SNR of 48.70 in Fig. 26. The three panels show the reconstructed ASDs for the SGWB and for the instrumental noise and the total, which is the sum of the three. No foreground has been considered in this case. In Fig. 27, we show corresponding results for a power law with a higher SNR of 971.

We see that our ability to reconstruct the signal component of the data stream is poor when the SNR is low. However, we can obtain good measurements of

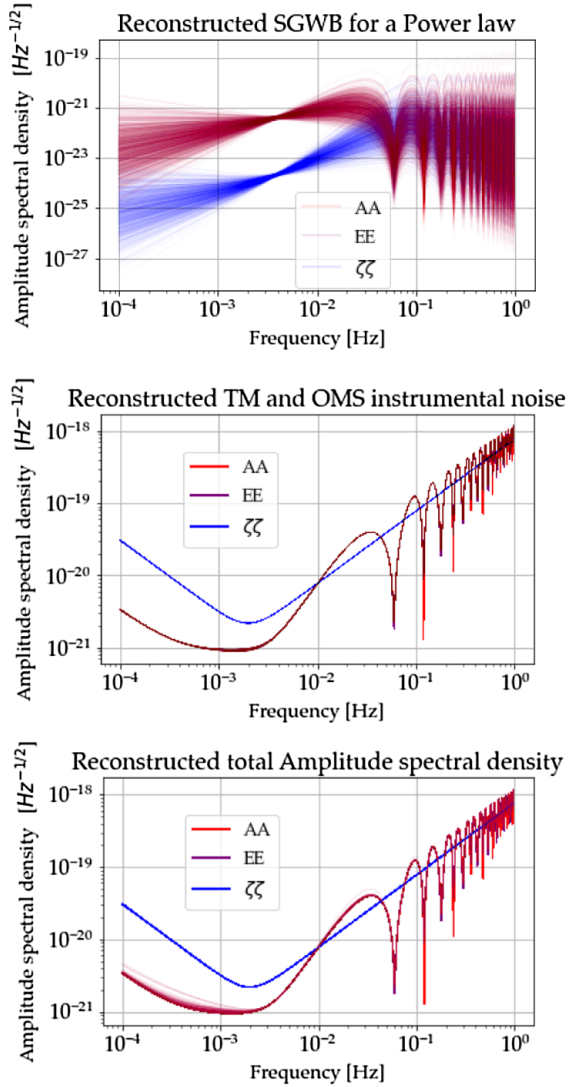


FIG. 26. Signal and noise reconstruction for a power law SGWB with SNR 48.70. We show the signal and noise PSDs corresponding to random draws from the posterior, approximated using the Fisher matrix as described in the text. In each panel, the curves correspond to the three TDI channels:  $A$  (blue),  $E$  (red), and  $\zeta$  (green). Upper panel: reconstructed SGWB; middle panel: reconstructed instrumental noise; lower panel: total reconstructed ASD (signal + noise).

the instrumental noise and the total spectral density. We note that the total ASD reconstruction in the lower panel in Fig. 26 is somewhat poorer than the noise-only component, which does not fit with the expectation that we are measuring the total. This happens due to the breakdown in the Fisher matrix approximation for the SGWB parameters in this case, because the SGWB parameter uncertainties are large and no longer in the linear signal regime. At higher SNR, we start to be able to reconstruct the SGWB more precisely, shown by a reduction in the scatter in Fig. 27. As the SNR is increased, we would expect the scatter to reduce further. The reconstruction of the noise spectral density is comparable to what is seen in the lower SNR case, but we would eventually expect it to degrade as the SGWB becomes more dominant in the data. The

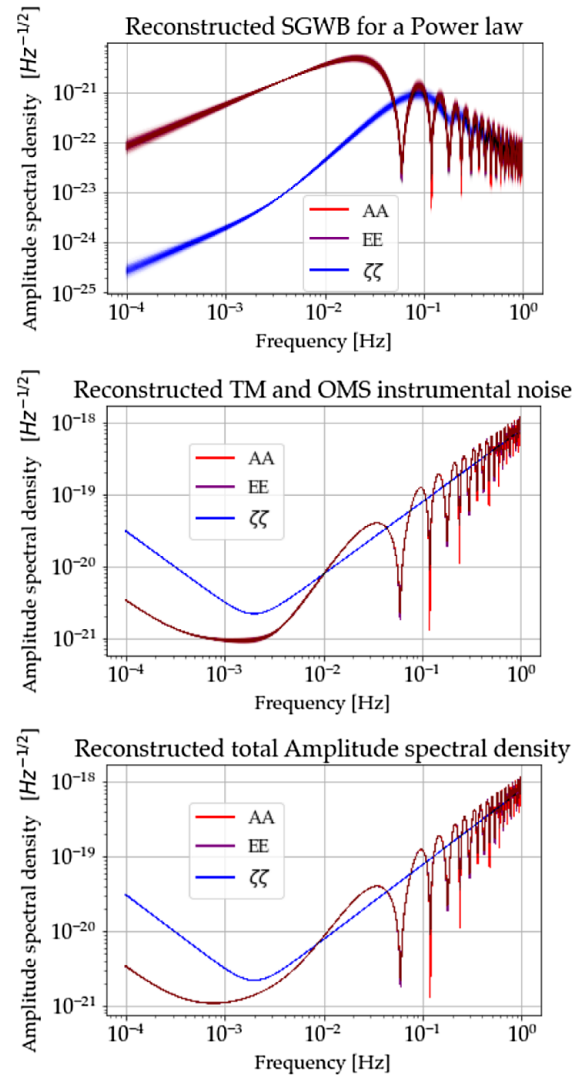


FIG. 27. As in Fig. 26 but for a power law background with higher SNR of 971.

reconstruction of the total spectral density is similar to the low SNR case but does not suffer from the scatter induced by the breakdown of the Fisher matrix approximation, as all uncertainties remain in the linear regime in this case.

In conclusion, it is also interesting to notice in the instrumental noise reconstruction that the channels  $A$  and  $E$  are affected by the SGWB in the range from 1 to 4 mHz, where the SGWB dominates the total spectral density, as might be expected.

- 
- [1] Pau Amaro-Seoane *et al.*, Laser interferometer space antenna, [arXiv:1702.00786](https://arxiv.org/abs/1702.00786).
- [2] Antoine Klein *et al.*, Science with the space-based interferometer eLISA: Supermassive black hole binaries, *Phys. Rev. D* **93**, 024003 (2016).
- [3] Davide Gerosa, Sizheng Ma, Kaze W. K. Wong, Emanuele Berti, Richard O’Shaughnessy, Yanbei Chen, and Krzysztof Belczynski, Multiband gravitational-wave event rates and stellar physics, *Phys. Rev. D* **99**, 103004 (2019).
- [4] Christopher J. Moore, Davide Gerosa, and Antoine Klein, Are stellar-mass black-hole binaries too quiet for LISA?, *Mon. Not. R. Astron. Soc.* **488**, L94 (2019).
- [5] Alberto Sesana, Prospects for multiband gravitational-wave astronomy after GW150914, *Phys. Rev. Lett.* **116**, 231102 (2016).
- [6] Stanislav Babak, Jonathan Gair, Alberto Sesana, Enrico Barausse, Carlos F. Sopuerta, Christopher P.L. Berry, Emanuele Berti, Pau Amaro-Seoane, Antoine Petiteau, and Antoine Klein, Science with the space-based interferometer LISA. V: Extreme mass-ratio inspirals, *Phys. Rev. D* **95**, 103012 (2017).
- [7] Chiara Caprini, Daniel G. Figueroa, Raphael Flauger, Germano Nardini, Marco Peloso, Mauro Pieroni, Angelo Ricciardone, and Gianmassimo Tasinato, Reconstructing the spectral shape of a stochastic gravitational wave background with LISA, *J. Cosmol. Astropart. Phys.* **11** (2019) 017.
- [8] Bruce Allen and Joseph D. Romano, Detecting a stochastic background of gravitational radiation: Signal processing strategies and sensitivities, *Phys. Rev. D* **59**, 102001 (1999).
- [9] Wen-Hong Ruan, Zong-Kuan Guo, Rong-Gen Cai, and Yuan-Zhong Zhang, Taiji program: Gravitational-wave sources, *Int. J. Mod. Phys. A* **35**, 2050075 (2020).
- [10] R. Abbott *et al.*, Upper limits on the isotropic gravitational-wave background from Advanced LIGO and Advanced Virgo’s third observing run, *Phys. Rev. D* **104**, 022004 (2021).
- [11] Olaf Hartwig, Marc Lilley, Martina Muratore, and Mauro Pieroni, Stochastic gravitational wave background reconstruction for a nonequilateral and unequal-noise LISA constellation, *Phys. Rev. D* **107**, 123531 (2023).
- [12] Lee S. Finn, Detection, measurement and gravitational radiation, *Phys. Rev. D* **46**, 5236 (1992).
- [13] Michele Vallisneri, Use and abuse of the Fisher information matrix in the assessment of gravitational-wave parameter-estimation prospects, *Phys. Rev. D* **77**, 042001 (2008).
- [14] M. Zanolin, S. Vitale, and N. Makris, Application of asymptotic expansions for maximum likelihood estimators errors to gravitational waves from binary mergers: The single interferometer case, *Phys. Rev. D* **81**, 124048 (2010).
- [15] M. Armano *et al.*, Sub-femto- $g$  free fall for space-based gravitational wave observatories: LISA pathfinder results, *Phys. Rev. Lett.* **116**, 231101 (2016).
- [16] Martina Muratore, Olaf Hartwig, Daniele Vetrugno, Stefano Vitale, and William Joseph Weber, Effectiveness of null time-delay interferometry channels as instrument noise monitors in LISA, *Phys. Rev. D* **107**, 082004 (2023).
- [17] J. W. Armstrong, F. B. Estabrook, and Massimo Tinto, Time-delay interferometry for space-based gravitational wave searches, *Astrophys. J.* **527**, 814 (1999).
- [18] Massimo Tinto and Olaf Hartwig, Time-delay interferometry and clock-noise calibration, *Phys. Rev. D* **98**, 042003 (2018).
- [19] Marie-Sophie Hartig, Sönke Schuster, and Gudrun Wanner, Geometric tilt-to-length coupling in precision interferometry: mechanisms and analytical descriptions, *J. Opt.* **24**, 065601 (2022).
- [20] S. Paczkowski, R. Giusteri, M. Hewitson, N. Karnesis, E. D. Fitzsimons, G. Wanner, and G. Heinzl, Postprocessing subtraction of tilt-to-length noise in LISA, *Phys. Rev. D* **106**, 042005 (2022).
- [21] Martina Muratore, Time delay interferometry for LISA science and instrument characterization, Ph.D. thesis, Trento University, 2021, [10.15168/11572\\_312487](https://doi.org/10.15168/11572_312487).
- [22] Olaf Hartwig, Instrumental modelling and noise reduction algorithms for the Laser Interferometer Space Antenna, Ph.D. thesis, Leibniz University, Hannover, 2021, [10.15488/11372](https://doi.org/10.15488/11372).
- [23] Raphael Flauger, Nikolaos Karnesis, Germano Nardini, Mauro Pieroni, Angelo Ricciardone, and Jesús Torrado, Improved reconstruction of a stochastic gravitational wave background with LISA, *J. Cosmol. Astropart. Phys.* **01** (2021) 059.
- [24] Matthew R. Adams and Neil J. Cornish, Discriminating between a stochastic gravitational wave background and instrument noise, *Phys. Rev. D* **82**, 022002 (2010).
- [25] Quentin Baghi, Nikolaos Karnesis, Jean-Baptiste Bayle, Marc Besançon, and Henri Inchauspé, Uncovering gravitational-wave backgrounds from noises of unknown shape with LISA, *J. Cosmol. Astropart. Phys.* **04** (2023) 066.
- [26] Etienne Savalle, Jonathan Gair, Lorenzo Speri, and Stanislav Babak, Assessing the impact of instrumental calibration uncertainty on LISA science, *Phys. Rev. D* **106**, 022003 (2022).

- [27] Stanislav Babak, Antoine Petiteau, and Martin Hewitson, LISA sensitivity and SNR calculations, [arXiv:2108.01167](https://arxiv.org/abs/2108.01167).
- [28] Lorenzo Sala, Residual test mass acceleration in LISA Pathfinder: in-depth statistical analysis and physical sources, Ph.D. thesis, University of Trento, 2023, [10.15168/11572\\_384049](https://doi.org/10.15168/11572_384049).
- [29] M. Armano *et al.*, Transient acceleration events in LISA pathfinder data: Properties and possible physical origin, *Phys. Rev. D* **106**, 062001 (2022).
- [30] M. Armano *et al.*, Beyond the required LISA free-fall performance: New LISA pathfinder results down to 20  $\mu\text{Hz}$ , *Phys. Rev. Lett.* **120**, 061101 (2018).
- [31] M. Tinto and S. V. Dhurandhar, Time-delay interferometry, *Living Rev. Relativity* **24** 1 (2021).
- [32] Daniel A. Shaddock, Operating LISA as a sagnac interferometer, *Phys. Rev. D* **69**, 022001 (2004).
- [33] Daniel A. Shaddock, Massimo Tinto, Frank B. Estabrook, and J. W. Armstrong, Data combinations accounting for LISA spacecraft motion, *Phys. Rev. D* **68**, 061303 (2003).
- [34] Massimo Tinto, F. B. Estabrook, and J. W. Armstrong, Time delay interferometry with moving spacecraft arrays, *Phys. Rev. D* **69**, 082001 (2004).
- [35] Thomas A. Prince, Massimo Tinto, Shane L. Larson, and J. W. Armstrong, LISA optimal sensitivity, *Phys. Rev. D* **66**, 122002 (2002).
- [36] Martina Muratore, Daniele Vetrugno, Stefano Vitale, and Olaf Hartwig, Time delay interferometry combinations as instrument noise monitors for LISA, *Phys. Rev. D* **105**, 023009 (2022).
- [37] Olaf Hartwig and Martina Muratore, Characterization of time delay interferometry combinations for the LISA instrument noise, *Phys. Rev. D* **105**, 062006 (2022).
- [38] M. Chwalla, K. Danzmann, M. Dovale Álvarez, J. J. Esteban Delgado, G. Fernández Barranco, E. Fitzsimons, O. Gerberding, G. Heinzel, C. J. Killow, M. Lieser, M. Perreux-Lloyd, D. I. Robertson, J. M. Rohr, S. Schuster, T. S. Schwarze, M. Tröbs, G. Wanner, and H. Ward, Optical suppression of tilt-to-length coupling in the LISA long-arm interferometer, *Phys. Rev. Appl.* **14**, 014030 (2020).
- [39] Olaf Hartwig and Jean-Baptiste Bayle, Clock-jitter reduction in LISA time-delay interferometry combinations, *Phys. Rev. D* **103**, 123027 (2021).
- [40] Martina Muratore, Daniele Vetrugno, and Stefano Vitale, Revisitation of time delay interferometry combinations that suppress laser noise in LISA, *Classical Quantum Gravity* **37**, 185019 (2020).
- [41] Allen Nussbaum, Group theory and normal modes, *Am. J. Phys.* **36**, 529 (1968).
- [42] Martina Muratore and Jonathan Gair, [https://github.com/martinaAEI/noise\\_knowledge\\_uncertainty](https://github.com/martinaAEI/noise_knowledge_uncertainty).
- [43] Jean-Baptiste Bayle, Aurélien Hees, Marc Lilley, and Christophe Le Poncin-Lafitte, LISA orbits (2022), [10.5281/zenodo.6412992](https://doi.org/10.5281/zenodo.6412992).
- [44] LISA red-book (to be published).
- [45] Chiara Caprini and Daniel G. Figueroa, Cosmological backgrounds of gravitational waves, *Classical Quantum Gravity* **35**, 163001 (2018).
- [46] Stanislav Babak, Chiara Caprini, Daniel G. Figueroa, Nikolaos Karnesis, Paolo Marcoccia, Germano Nardini, Mauro Pieroni, Angelo Ricciardone, Alberto Sesana, and Jesús Torrado, Stochastic gravitational wave background from stellar origin binary black holes in LISA, *J. Cosmol. Astropart. Phys.* **08** (2023) 034.
- [47] Leonard Lehoucq, Irina Dvorkin, Rahul Srinivasan, Clement Pellouin, and Astrid Lamberts, Astrophysical uncertainties in the gravitational-wave background from stellar-mass compact binary mergers, *Mon. Not. R. Astron. Soc.* **526**, 4378 (2023).
- [48] N. Bartolo, V. De Luca, G. Franciolini, A. Lewis, M. Peloso, and A. Riotto, Primordial black hole dark matter: LISA serendipity, *Phys. Rev. Lett.* **122**, 211301 (2019).
- [49] N. Bartolo, V. De Luca, G. Franciolini, M. Peloso, D. Racco, and A. Riotto, Testing primordial black holes as dark matter with LISA, *Phys. Rev. D* **99**, 103521 (2019).
- [50] G. Franciolini, Primordial black holes: From theory to gravitational wave observations, [arXiv:2110.06815](https://arxiv.org/abs/2110.06815).
- [51] Nicola Bartolo *et al.*, Science with the space-based interferometer LISA. IV: Probing inflation with gravitational waves, *J. Cosmol. Astropart. Phys.* **12** (2016) 026.
- [52] Chiara Caprini, Mark Hindmarsh, Stephan Huber, Thomas Konstandin, Jonathan Kozaczuk, Germano Nardini, Jose Miguel No, Antoine Petiteau, Pedro Schwaller, Géraldine Servant, and David J. Weir, Science with the space-based interferometer eLISA. II: Gravitational waves from cosmological phase transitions, *J. Cosmol. Astropart. Phys.* **04** (2016) 001.
- [53] Mark Hindmarsh, Stephan J. Huber, Kari Rummukainen, and David J. Weir, Shape of the acoustic gravitational wave power spectrum from a first order phase transition, *Phys. Rev. D* **96**, 103520 (2017).
- [54] Nikolaos Karnesis, Stanislav Babak, Mauro Pieroni, Neil Cornish, and Tyson Littenberg, Characterization of the stochastic signal originating from compact binary populations as measured by LISA, *Phys. Rev. D* **104**, 043019 (2021).
- [55] Eric Thrane and Joseph D. Romano, Sensitivity curves for searches for gravitational-wave backgrounds, *Phys. Rev. D* **88**, 124032 (2013).
- [56] LISA Pathfinder Collaboration, In-depth analysis of LISA Pathfinder performance results: Time evolution, noise projection, physical models and implications for LISA.
- [57] N. Karnesis, M. Lilley, and A. Petiteau, Assessing the detectability of a stochastic gravitational wave background with LISA, using an excess of power approach, *Classical Quantum Gravity* **37**, 215017 (2020).
- [58] B. Picinbono, Second-order complex random vectors and normal distributions, *IEEE Trans. Signal Process.* **44**, 2637 (1996).